Ferroelectric Domain and Switching Dynamics in Curved In_2Se_3: First Principle and Deep Learning Molecular Dynamics Simulations

[‡]Dongyu Bai[1], Yihan Nie[2,1], Jing Shang[3], Junxian Liu[1], Minghao Liu[1], Yang Yang[4], Haifei Zhan[2], Liangzhi Kou[1*] and Yuantong Gu[1*]*

1. School of Mechanical, Medical and Process Engineering, Queensland University of Technology, Brisbane, QLD 4001, Australia

2. College of Civil Engineering and Architecture, Zhejiang University, Hangzhou 310058, China

3. School of Materials Science and Engineering, Shaanxi University of Science and Technology, Xi'an, 710021 China

4. State Key Laboratory for Mechanical Behavior of Materials, Xi'an Jiaotong University, Xi'an 710049, China

Abstract

Despite its prevalence in experiments, the influence of complex strain on material properties remains understudied due to the lack of effective simulation methods. Here, the effects of bending, rippling, and bubbling on the ferroelectric domains are investigated in In_2Se_3 monolayer by density functional theory and deep learning molecular dynamics simulations. Since the ferroelectric switching barrier can be increased (decreased) by tensile (compressive) strain, automatic polarization reversal occurs in α-In_2Se_3 with strain gradient when it is subjected to the bending, rippling, or bubbling deformations, to create localized ferroelectric domains with varying sizes. The switching dynamics depends on the magnitude of curvature and temperature, following an Arrhenius-style relationship. This study not only provides a promising solution for cross-scale studies using deep learning but also reveals the potential to manipulate local polarization in ferroelectric materials through strain engineering.

Keywords: 2D ferroelectric, α-In_2Se_3, polarization switching, deep learning potential, strain engineering

Over the past two decades, 2D materials have emerged as a new research hotspot, due to their unique physical and chemical properties, as well as promising applications in biosensors,[1, 2] solar photovoltaics,[3] catalysis,[4-6] electronic devices[7-9]. The atomic-thick structures distinguish them from their bulk counterparts in terms of mechanical, thermal and electrical properties. However, the weaker bending stiffness compared to their in-plane modulus[10] makes them easy to induce out-of-plane bending and crumpling, especially when influenced by the substrate,[11-13] interface liquid,[14, 15] and thermal strain.[16-18] In fact, the inevitable wrinkled structures have been commonly observed in graphene,[19] transition metal dichalcogenides,[20] and black phosphorene. The corrugations have been shown to significantly affect the electronic, mechanical, electrical, and optical properties, thereby impacting the performance of associated devices.[21, 22] For example, the crest of graphene's nano-bubbles exhibits enhanced catalytic activity for HER or ORR[23, 24] than the area of flat graphene. The rippling deformation in MoS_2 has detrimental effects on electron mobility, removing them could result in optimal performance of electronic device. Through proper strain engineering, the out-of-plane deformation can be used for optimizing performance or designing novel functional devices.[25, 26]

2D ferroelectrics, such as In_2Se_3,[27-29] $MoTe_2$,[30] $CuInP_2S_6$,[31-33] and the SnTe family,[34-36] are a unique class of van der Waals materials that exhibit stable spontaneous and switchable polarization under external stimuli. Mechanical bending or rippling deformation can well couple with electric polarization due to the generated interlayer movement or ion migration,[27, 37] leading to flexoelectric phenomena or ferroic domains that enable the measurement of strain gradient in mechanical structures electrically. Rippling/bending deformations therefore gain the ability to weaken, strengthen, or reverse polarization. For example, polarization vortex or polar skyrmions were realized at room temperature in ferroelectric bubbling domains induced by lattice mismatch strain in $(PbTiO_3)_n/(SrTiO_3)_n$ heterostructures.[38, 39] Ripple-induced ferroic

phase transition and domain switching have been observed in 2D ferroelectric GeSe layers, indicating their potential application in flexible electronics.[40] Despite their fundamental and practical importance, a deep understanding at the atomic level for the effect of wrinkles on polarization switching, especially in terms of out-of-plane ferroelectricity, remains scarce due to the lack of appropriate simulation methods and the requirements on extreme-high resolution of experimental measurements.

Here, we revealed the impacts of bending, rippling and bubbling deformations of α-In_2Se_3 on its ferroelectric polarization, based on density functional theory (DFT) and molecular dynamics (MD) simulations. The methodology details can be found in Supporting Information & Fig. S1. It is found that the ferroelectric switching barrier can be reduced/increased by uniaxial tensile/compressive strain, which enables the automatic polarization reversal when tensile and compressive strains coexist. The switching dynamics in complex strain deformation is then studied with deep-learning potentials and large scale MD simulations.[41-43] Ferroelectric domains can be created and switched by the rippling and bubbling deformations, and the switching time is dependent on curvature and temperature. Our results provide a new approach for the strain engineering of 2D ferroelectric materials as flexible electronic devices.

Switching Barrier Influenced by Strain

The spontaneous polarization in α-In_2Se_3 results from structural asymmetry along the out-of-plane direction, where the position of the central Se layer plays a critical role in deciding polarization orientation. Two steps in-plane shift of the central Se layer (ionic displacement) to overcome an energy barrier of 67 meV can cause the polarization reverse (Supporting Information, Fig. S3b). The calculation is conducted within a lattice cell, and in a multi-lattice system influenced by the nucleation-growth mechanism, the energy barrier could experience further reduction compared to the unit cell DFT results.[27, 44]

We first investigate the impact of uniaxial ±3% strain on the energy barrier, to lay theoretical foundation for later analysis of complex strain although it is probably challenging to achieve -3% compressive strain in reality. DFT calculation indicates that the energy barrier of ferroelectric switching can be significantly increased by the tensile strain. The value can be increased by ~300% (**Fig. 1a**) with 3% tensile strain, but reduced to 0 with -3% compressive strain, implying that the polarization is easier/more difficult to switch under the compression/tensile strain. Different exchange correlation functions have the impacts on the values of ferroelectric switching, but don't affect the conclusion, See Fig. S2. The phenomena can be intuitively understood from structural deformation, where the thickness along out-of-plane direction will expand under in-plane compression deformations, to facilitate the motion of the Se layer. This can also be seen from electron localization function (ELF) (Fig. 1c). Taking the P↑ In_2Se_3 as an example, more localization of electron is observed in tensile case (+3%) than that in compressive model (-3%). Thus, the tensile state is less prone to switch polarization direction than the compressed state.

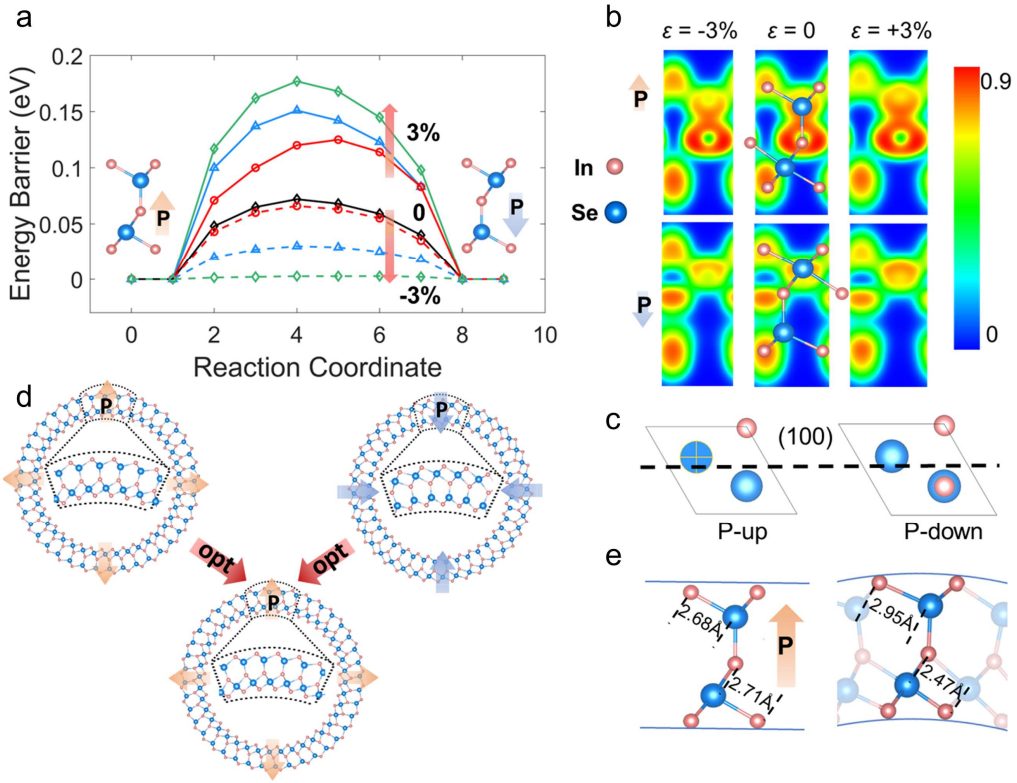

Fig. 1. (a) Polarization switching barriers of monolayer α-In_2Se_3 under various in-plane strains. (b) The electron localization function (ELF) maps under in-plane strains. The upper and lower panels present the P↑ and P↓ In_2Se_3 respectively. (c) The atomic structures of cross section corresponding to ELF maps of P↑ and P↓. (d) The initial and optimized structures of In_2Se_3 nanotube from P↑ and P↓ states. (e) The variation of In-Se bond length before and after bending a nanotube with a radius of 22.60 Å.

To verify the impacts of strain on the ionic displacement and associated phase transition, the In_2Se_3 nanotube with the radius of 22.6 Å is built to investigate the bending effect. 15 Å of vacuum layer is added in the radial direction, while periodicity is applied in the axial direction. Depending on the wrap direction, two models with initially opposite polarization states are constructed (Fig. 1d). After the optimization, both are transformed into the same configuration, i.e., the polarization pointing towards outside as shown in Fig. 1d. Due to the structural symmetry, the nanotube exhibits overall zero polarization and internal electric field due to the cancellation. The In-Se bond lengths are stretched to 2.95 Å at the outer layer (originally 2.68 Å), but compressed to 2.47 Å (originally 2.71 Å) at inner layer (Fig. 1e). The outside of the tube is subjecting the tensile strain while the inner side is subjecting the compressive strain. The central Se layer tends to move to the compression region, since the polarization switching barrier is significantly lower under compressive strain as found in Fig. 1a. Therefore, regardless of the initial polarization direction and structural models, the polarization direction in In_2Se_3 tubes always points outwards after the structural optimization, and the central Se layer prefers to migrate to the compression side under bending conditions when both tensile and compressive strains coexist. Besides the ionic displacement induced polarization reversal, it is worthy to notice that the flexoelectric effect from bending induced strain gradient is also a potentially trigger for polarization switching as found in MoS_2[45-47]. We therefore calculate the polarization

contribution in bent In_2Se_3 induced by flexoelectric effect to elucidate the primary mechanism behind polarization reversal. Calculations demonstrate that at a curvature radius of 22.60 Å, the flexoelectric effect-induced polarization accounts for 24.29% of the overall polarization value. The proportion significantly diminishes as a function of the reciprocal of the radius, reaching only 10.98% at a curvature radius of 50 Å. This indicates that the dominant mechanism governing polarization switching is ionic displacement (the shift in the central Se layer), but not flexoelectric effect (refer to Fig. S4 & S5). Given that the curvature radius is much larger in rippling and bubbling deformations (see below), we will disregard the flexoelectric-induced polarization and reversal in the subsequent analysis.

Validation of Deep Learning Potential

To study complex strain and non-uniform deformation, we developed the force fields of In_2Se_3 with the DeepMD-kit.[41] The training set is based on open-source data from the recent work by Wu et al,[48] which was generated by DP-GEN and contained 22600 monolayer structures such as α, β, β',β'_1, and β'_2 phases and 2163 bulk structures. Besides DeepMD and DP-GEN, the alternative choice can be active learning machine learning potentials packages that can accelerate the database setup process. [49, 50] Details of the potential training including the descriptor, training neuron layers and accuracy can be found from the Supporting information 1. Our benchmark calculations indicate that the potential performs remarkably well in both energy and force predictions. Across nearly 8,500 examples, the mean absolute error (MAE) is around 3.9 meV/atom (Fig. S4). Significantly, the deep learning potential can accurately predict the energy barrier under various strain conditions and phase transitions, demonstrating remarkable consistency with previous DFT results (Fig. S2， S6 & S7). All MD simulations below are based on this deep learning-force field and implemented in LAMMPS software.

Switching Dynamics under Pure Bending

Although DFT simulation can accurately predict the polarization reversal behaviors, it doesn't consider thermal disturbance from the environments. Based on the trained force field, we are able to study the switching dynamics and complex systems at various temperatures. We first study the In_2Se_3 nanotube with radius of 28.25 Å from the MD simulation. Consistent with DFT simulations, the polarization which initially points inside is reversed after the structural relaxation, with a sudden energy drop, as seen in **Figs. 2a** &. S8. The switching time τ (defined as the time for the total energy reduces to the average energy of the two states) is 17 ps at 370 K (Fig. 2a), but reduces to 10 ps when the temperature was increased to 380 K, indicating the switching process is accelerated by the increased thermal disturbance. The underlying mechanism can be attributed to increased kinetic energy of the atoms, which enhances the likelihood of overcoming the energy barrier and accelerates ferroelectric switching. The switching time τ exhibits an exponential relationship with temperature, see Fig. 2c. Since the process is akin to chemical reactions, where the energy barrier of ferroelectric switching corresponds to the activation energy, the switching time should be the reciprocal of the reaction rate. It could be thus effectively modeled using an Arrhenius-style equation:

$$\tau = Ae^{\left(\frac{E_b}{k_b T}\right)} + t_m \quad (1)$$

where A is the amplitude fitted as 9.57×10^{-12} ps, E_b is the energy barrier fitted as 0.895eV and constant t_m equals 1.90 ps, k_b is the Boltzmann constant, and T is the temperature. The constant t_m indicates that for a certain curvature, there is a minimal time to achieve the switching process.

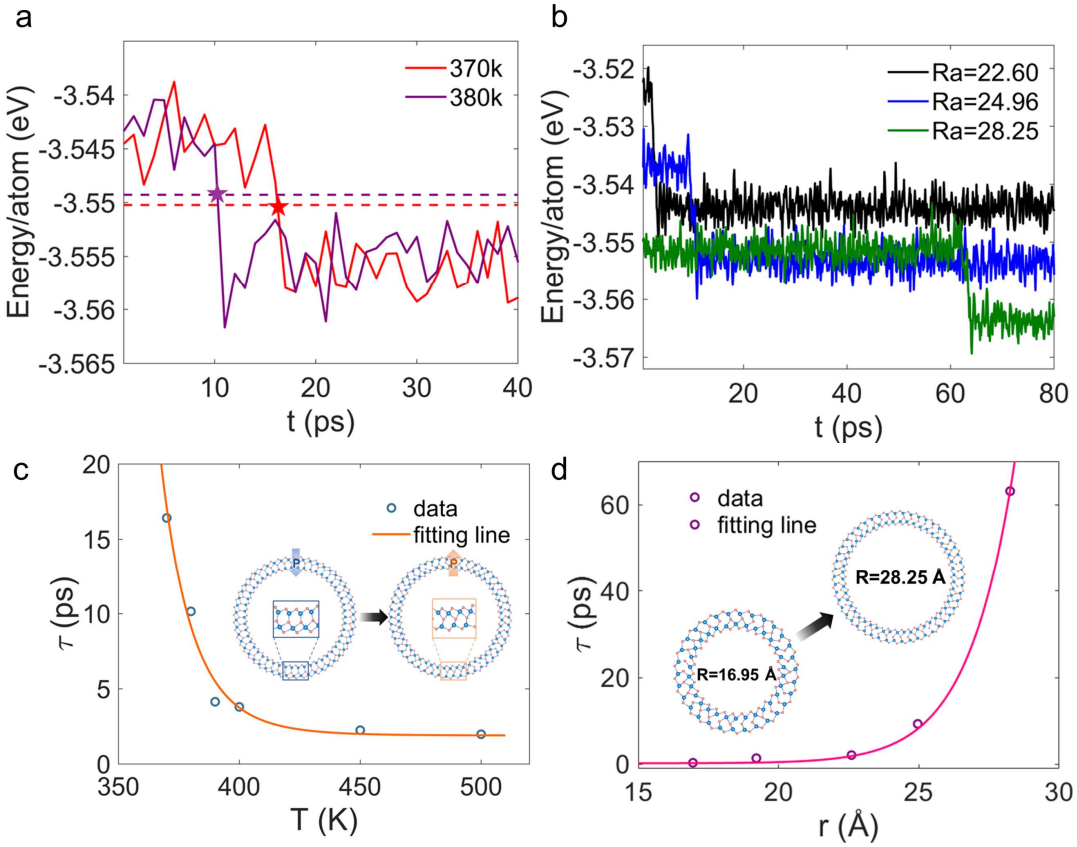

Fig. 2. DLMD results for In_2Se_3 nanotubes. (a) Energy variation for a tube with radius 28.25 Å at different temperatures, represented by the solid line. The dashed line is the average value between the two polarization states. (b) Energy variations with time for nano tubes with radius from 22.60 Å to 28.25 Å at 300 K. (c) Switching time τ as a function of temperature and its fitting curve for nanotube with radius of 28.25 Å. The insets are the nanotube configurations before and after the polarization switching. (d) Switching time τ as a function of different radii and its fitting curve for nanotube at 300 K. The illustration is the configurations of tubes with a radius of 16.95 Å and 28.25 Å after the polarization switching.

Another factor affecting the switching dynamics is the bending curvature. The switching time τ for nanotubes with radius of 22.6 Å, 24.96 Å, and 28.25 Å are simulated under 300 K (Figs. 2b & S9) to study the size effect. The polarization reversal takes 3 ps for the smallest tube (R=22.6 Å), but much longer for the other two (10 ps for R=24.96 Å and 63 ps for R=28.25

Å respectively). After taking the curvature radius into the consideration, the Arrhenius-style equation (Eq. 1) can be revised and updated as below:

$$\tau = B\, e^{\frac{l_e\sqrt{r}}{k_b T}} + t_m \quad (2)$$

where E_b in the equation 1 can be replaced as $l_e\sqrt{r}$. The amplitude B equals 6.245×10^{-14} ps, l_e is the coefficient for energy barrier 0.168 eV/Å$^{\frac{1}{2}}$, r is radius of nanotube model, and t_m equals 0.25 ps, as a minimal time for switching process at 300 K. The fitting equation indicates a linear relationship between the energy barrier and the 1/2 power of the radius of curvature, see Fig. 2d. Both equations give the similar energy barrier prediction values, i.e., 0.89 eV, for the nanotube with radius of 28.25 Å.

Switching Dynamics with Rippling Deformation and the Lifetime of the Transient Polarization

Rippling deformation is commonly observed in 2D materials when experiencing compression forces at the boundary. Here, a mono-sinusoidal shaped model with periodic boundary conditions in the in-plane direction is created to mimic rippling deformation. The thermal impacts of temperatures (ranging from 300 K to 670 K) and size effects of rippling amplitudes (m =15 and m = 20 Å) are studied. After the structural relaxation, a prominent phase transition occurs in the left region, which is situated in the wave trough with a positive curvature. This phase transition is caused by the ionic displacement of the central Se layer, resulting in a polarization switching from [0 0 1] to [0 0 -1], similar to the phenomenon observed in nanotubes (Fig. 2). In contrast, the polarization in the right region, located at the wave crest with a negative strain curvature, remains unchanged throughout the process. Therefore, the local polarization and induced electric field due to the non-uniform distribution have opposite preference direction in the two regions, resulting in localized ferroelectric domains. They are separated by the boundary (dashed line in Fig. 3a) characterized with paraelectric β phase, as indicated by the enlarged local structure. These structural phase

transitions and localized polarization reversals are also observed in other models with different rippling amplitudes (m=15 Å) and temperatures (Fig. S10 & S11).

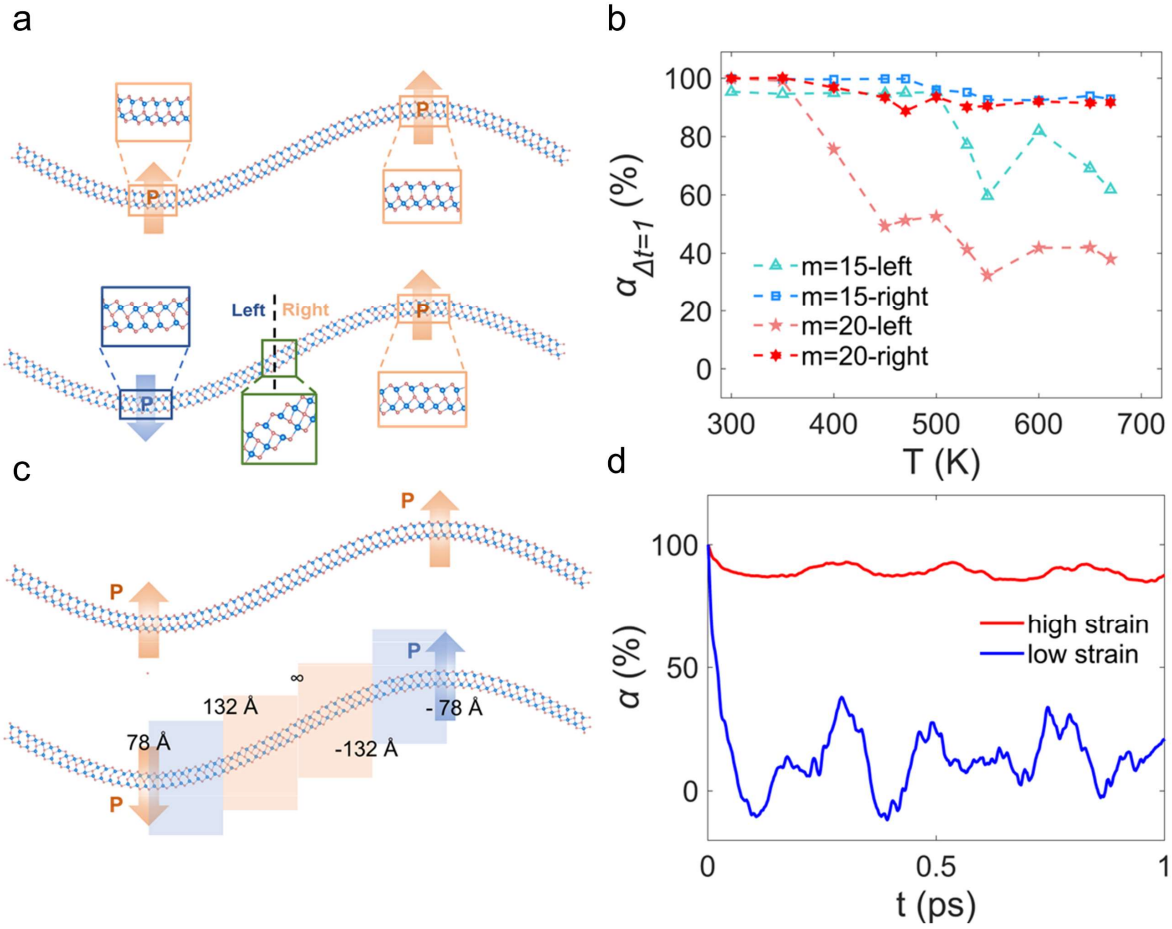

Fig. 3. Ferroelectric domain and dynamics in rippling models. (a) The monolayer rippling configuration with m=20 Å at 450 K. The top/bottom image represents the structure at 0/85 ps. (b) The polarization correlation of left and right regions at 1 ps as a function of temperature. (c) Division of the rippling model into high strain and low strain regions, with corresponding curvature radii indicated. (d) Temporal variation of polarization correlation in different strain regions.

As a dynamic process, the local polarization lifetime and the stability of ferroelectric domains are investigated by tracking the auto-correlation functions of local momentum. The method has been employed to experimentally measure the lifetime of polarization from voltage-modulated

scanning force microscopy which can analyze transient local polarization and subsequently process the obtained data mathematically .[51] The autocorrelation function is defined as

$$\alpha(t) = \frac{<\int \overrightarrow{D_i}(t_0)\overrightarrow{D_i}(t_0+t)dt_0>}{\alpha_i(0)} \quad (3)$$

to describe the proportion of polarization that can maintain its original direction over the time interval of t. $\overrightarrow{D_i}(t_0)$ is the value of the dipole moment of chunk i at t_0. t is the time interval. The autocorrelation function at the starting point $\alpha_i(0)$ is normalized to 1, namely all the polarizations at the beginning point to the same direction. After the time interval (1ps in Fig. 3b), we calculate the ratio which preserve the original direction (namely the autocorrelation), a low/high value indicates a short/long lifetime of the ferroelectric domain. **Fig. 3a** illustrates the polarization switching behavior in the ripple model before and after structural relaxation, the different autocorrelation functions are observed at left and right regions. The autocorrelation at the left region remains almost unchanged until temperature reaches 500K when the ripple attitude m=15 Å, but significantly decreases to around 60% at 550K. In contrast, it maintains as a constant value in the right region even the temperature is increased to 700K. The results imply that polarization reversal occurs only at the ripple wave trough after 1ps when reaching a critical temperature, but not at the wave crest (Fig. 3b). This finding holds true at larger rippling amplitude like m=20 Å. However, both the critical temperature (350K) and autocorrelation (only 30% at 550K) in the left region are much lower than the corresponding values when m=15 Å. Consequently, ripple amplitude can thus act as an effective parameter to facilitate the polarization switching and control the lifetime of ferroelectric domain.

Since ripple deformation will lead to a complex and non-uniform strain distribution, we also analyze and compare the transient polarization behavior in regions with different curvatures. Following relaxation, the ripple model with m=20 Å is divided into several distinct areas as shown in Fig. 3c. The radius of curvature falls between 78 Å and 132 Å in the high-

strain region, but exceeds 132 Å in the low-strain region. The calculated autocorrelation at 450 K, clearly illustrates that the polarization lifetime in the high-strain region is notably longer than that in the low-strain region, with the latter being like transient polarization behavior (Fig. 3d).

Switching Dynamics with Bubbling Deformation and the Ferroelectric Domain

For bubbling deformation, it is mimicked by the dual sinusoidal model with similar boundary conditions as ripple model. More details about the models and calculation methods can be found in Supporting Information 2&3.

As shown in **Fig. 4a**, the polarization distribution at 450 K is presented, for the bubble amplitudes of 11 Å, 13 Å and 15 Å. After 30ps structural relaxation for the model with m=11 Å, the adjacent twin domains are found with clear opposite polarizations, as indicated by red and blue colors. Although the polarizations at the boundary regions are affected by thermal fluctuations, the overall distribution can be well-maintained up to 50 ps. When the bubble amplitude is increased to 13 Å or 15 Å, the continuity of ferroelectric domain is noticeably diminished. The crest (trough) still exhibits positive (negative) polarization although the domain size obviously shrinks.

The influence of bubble amplitude on the continuity of polarization domain size can be intuitively confirmed by image autocorrelation analysis, as shown in the bottom panels of Fig. 4a. Brighter regions indicate a higher degree of self-similarity and stronger correlation, corresponding to the areas with the larger size of the polarization domain or the continuity of the polarization domain. It is found that, an increased m results in a decrease in brightness at the crest of the autocorrelation image, indicating the disruption of the continuity of the

polarized domains or a reduction in the size of the positively polarized domains at the crest (Fig S12).

The examination of relaxation studies at various temperatures reveals its substantial influence on ferroelectric domains, wherein higher temperatures notably diminish the size of the local polarization domain, see Fig. 4b & Fig. S13. For instance, at 800 K, the local polarization distribution is disrupted after 50 ps structural relaxation, leading to a homogenous mixture and uniform distribution of different domain because the ferroelectricity of In_2Se_3 disappeared over curie temperature[52].

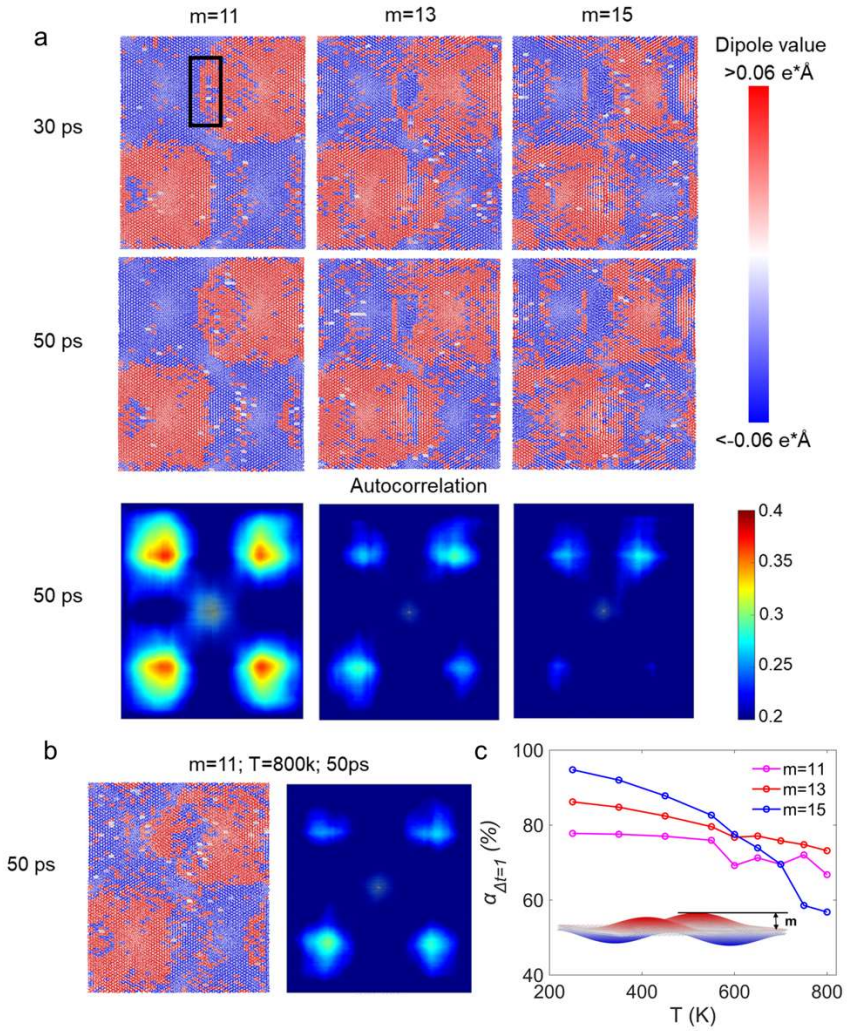

Fig. 4. (a) The polarization distribution during relaxation and autocorrelation maps at m=11, 13 and 15 at 450 K in bubbling model. The boundary of the domain is the intersection between

the red and blue regions, using the image contained within the rectangular box as an illustrative example. (b) The polarization distribution at 50 ps and autocorrelation map at m=11 at 800 K in bubbling model. (c) Structural stability $\alpha_{\Delta t=1}$ of different m with temperature and its trend line in bubbling model.

The influence of temperature and bubbling amplitude on the ferroelectric domain can be more clearly seen when we specifically exclude the impact of tensile effects. Here, the autocorrelation function is utilized to analyze the polarization lifetime within the high-strain region of the bubbling model (Figs. S14, S15 & Fig. 4c). Under the same strain condition, $\alpha_{\Delta t=1}$ exhibits lower values at higher temperatures, indicating that local polarization stability decreases when temperature increases. Concurrently, the bubbling amplitude demonstrates a positive impact on stability under consistent temperature conditions. An increased strain gradient (corresponding to an increased bubbling amplitude value) leads to a higher $\alpha_{\Delta t=1}$, namely the longer lifetime in the polarization domain. For example, the value is 77% when m=11 Å at 250 K, but increases to 86% and 94% as the amplitude m = 13 Å and 15 Å respectively. These results confirm that in the large bubbling model of In_2Se_3, previous relation between polarization stability and curvature still remains.

In summary, we report the polarization switching and its dynamics in curved In_2Se_3 through the joint DFT and DLMD simulations. Ferroelectric In_2Se_3 will undergo an automatic polarization reversal under the pure bending, the switching time is dependent on the environmental temperature and bending curvature. Research conducted using complex rippling and bubbling models reveals that lower temperatures and elevated bending strain foster larger domain sizes and longer lifetimes. Our research offers a promising approach for investigating strain effect on polarization dynamics of ferroelectric materials by conducting cross-scale simulations, and it provides valuable insights for the controlling polarization characteristics of ferroelectric materials by strain engineering in device fabrication.

ASSOCIATED CONTENT

Supporting Information

The Supporting Information are available free of charge at .

Details for DL potential training, methods of model construction, computational details of DFT and MD simulations, validation results for DL potential, additional results for nanotube, rippling and bubbling models (PDF)

AUTHOR INFORMATION

Corresponding Authors

Yihan Nie – *College of Civil Engineering and Architecture, Zhejiang University, Hangzhou 310058, China; School of Mechanical, Medical and Process Engineering, Queensland University of Technology, Garden Point Campus, Brisbane, QLD 4001, Australia;* Email: Yihan.nie@zju.edu.cn

Yuantong Gu – *School of Mechanical, Medical and Process Engineering, Queensland University of Technology, Garden Point Campus, Brisbane, QLD 4001, Australia;* Email: yuantong.gu@qut.edu.au

Liangzhi Kou – *School of Mechanical, Medical and Process Engineering, Queensland University of Technology, Garden Point Campus, Brisbane, QLD 4001, Australia;* Email: Liangzhi.kou@qut.edu.au

Authors

Dongyu Bai – *School of Mechanical, Medical and Process Engineering, Queensland University of Technology, Garden Point Campus, Brisbane, QLD 4001, Australia*

Jing Shang – *School of Materials Science and Engineering, Shaanxi University of Science and Technology, Xi'an, 710021 China*

Junxian Liu – *School of Mechanical, Medical and Process Engineering, Queensland University of Technology, Garden Point Campus, Brisbane, QLD 4001, Australia*

Minghao Liu – *School of Mechanical, Medical and Process Engineering, Queensland University of Technology, Garden Point Campus, Brisbane, QLD 4001, Australia*

Yang Yang – *State Key Laboratory for Mechanical Behavior of Materials, Xi'an Jiaotong University, Xi'an, 710049 China*

Haifei Zhan – *College of Civil Engineering and Architecture, Zhejiang University, Hangzhou 310058, China*

Author Contributions

L.K. conceived the idea and supervised the research with Y.G. and Y.N.. D.B. and Y.N. jointly designed the simulation process and models. D.B. trained the DLMD potential and conducted the MD simulations, assisted by Y.Y. and H.Z.. J.S., J.L. and M.L. executed the DFT simulations. D.B. analyzed the data and composed the manuscript. All authors have given approval to the final version of the manuscript.

ACKNOWLEDGMENTS

This work was supported by the Australian Research Council (Grant IC190100020 and DP200102546), the National Natural Science Foundation of China (Grant 12202254), and the High-performance Computing (HPC) resources provided by Queensland University of

Technology (QUT). This research was undertaken with assistance of resources and services from the National Computational Infrastructure (NCI), which is supported by the Australian Government.

ABBREVIATIONS

HER, hydrogen evolution reaction; OER, oxygen evolution reaction; DFT, density functional theory; DLMD, deep learning molecular dynamics;

Reference

(1) Lei, Z. L.; Guo, B. 2D Material-Based Optical Biosensor: Status and Prospect. *Adv. Sci.* **2022**, *9* (4), 2102924.
(2) Chen, F.; Tang, Q.; Ma, T.; Zhu, B.; Wang, L.; He, C.; Luo, X.; Cao, S.; Ma, L.; Cheng, C. Structures, properties, and challenges of emerging 2D materials in bioelectronics and biosensors. *InfoMat* **2022**, *4* (5), e12299.
(3) Das, S.; Pandey, D.; Thomas, J.; Roy, T. The role of graphene and other 2D materials in solar photovoltaics. *Adv. Mater.* **2019**, *31* (1), 1802722.
(4) Shifa, T. A.; Wang, F.; Liu, Y.; He, J. Heterostructures based on 2D materials: A versatile platform for efficient catalysis. *Adv. Mater.* **2019**, *31* (45), 1804828.
(5) Tang, L.; Meng, X.; Deng, D.; Bao, X. Confinement catalysis with 2D materials for energy conversion. *Adv. Mater.* **2019**, *31* (50), 1901996.
(6) Zhang, X.; Chen, A.; Chen, L.; Zhou, Z. 2D materials bridging experiments and computations for electro/photocatalysis. *Adv. Energy Mater.* **2022**, *12* (4), 2003841.
(7) Zhang, L.; Zhou, J.; Li, H.; Shen, L.; Feng, Y. P. Recent progress and challenges in magnetic tunnel junctions with 2D materials for spintronic applications. *Appl. Phys. Rev.* **2021**, *8* (2), 021308.
(8) Liu, Y.; Zeng, C.; Zhong, J.; Ding, J.; Wang, Z. M.; Liu, Z. Spintronics in two-dimensional materials. *Nanomicro Lett* **2020**, *12*, 1-26.
(9) Qi, L.; Ruan, S.; Zeng, Y.-J. Review on Recent Developments in 2D Ferroelectrics: Theories and Applications. *Adv. Mater.* **2021**, *33* (13), 2005098. DOI: https://doi.org/10.1002/adma.202005098.
(10) Zhang, Z.; Yang, Y.; Penev, E. S.; Yakobson, B. I. Elasticity, flexibility, and ideal strength of borophenes. *Adv. Funct. Mater.* **2017**, *27* (9), 1605059.
(11) Kim, J.; Park, H.; Hannon, J. B.; Bedell, S. W.; Fogel, K.; Sadana, D. K.; Dimitrakopoulos, C. Layer-resolved graphene transfer via engineered strain layers. *Science* **2013**, *342* (6160), 833-836.
(12) Jiang, Y.; Mao, J.; Duan, J.; Lai, X.; Watanabe, K.; Taniguchi, T.; Andrei, E. Y. Visualizing strain-induced pseudomagnetic fields in graphene through an hBN magnifying glass. *Nano Lett.* **2017**, *17* (5), 2839-2843.
(13) Reserbat-Plantey, A.; Kalita, D.; Han, Z.; Ferlazzo, L.; Autier-Laurent, S.; Komatsu, K.; Li, C.; Weil, R.; Ralko, A.; Marty, L. Strain superlattices and macroscale suspension of graphene induced by corrugated substrates. *Nano Lett.* **2014**, *14* (9), 5044-5051.
(14) Ghorbanfekr-Kalashami, H.; Vasu, K.; Nair, R. R.; Peeters, F. M.; Neek-Amal, M. Dependence of the shape of graphene nanobubbles on trapped substance. *Nat. Commun.* **2017**, *8* (1), 15844.
(15) Chen, Z.; Leng, K.; Zhao, X.; Malkhandi, S.; Tang, W.; Tian, B.; Dong, L.; Zheng, L.; Lin, M.; Yeo, B. S. Interface confined hydrogen evolution reaction in zero valent metal nanoparticles-intercalated molybdenum disulfide. *Nat. Commun.* **2017**, *8* (1), 14548.
(16) Jiang, H.; Khang, D.-Y.; Song, J.; Sun, Y.; Huang, Y.; Rogers, J. A. Finite deformation mechanics in buckled thin films on compliant supports. *Proc. Natl. Acad. Sci. U.S.A.* **2007**, *104* (40), 15607-15612.
(17) Chen, P. Y.; Sodhi, J.; Qiu, Y.; Valentin, T. M.; Steinberg, R. S.; Wang, Z.; Hurt, R. H.; Wong, I. Y. Multiscale graphene topographies programmed by sequential mechanical deformation. *Adv. Mater.* **2016**, *28* (18), 3564-3571.
(18) Zhang, Q.; Yin, J. Spontaneous buckling-driven periodic delamination of thin films on soft substrates under large compression. *Journal of the Mechanics and Physics of Solids* **2018**, *118*, 40-57.

(19) Huang, Y.; Wang, X.; Zhang, X.; Chen, X.; Li, B.; Wang, B.; Huang, M.; Zhu, C.; Zhang, X.; Bacsa, W. S. Raman spectral band oscillations in large graphene bubbles. *Phys. Rev. Lett.* **2018**, *120* (18), 186104.
(20) Brivio, J.; Alexander, D. T.; Kis, A. Ripples and layers in ultrathin MoS2 membranes. *Nano Lett.* **2011**, *11* (12), 5148-5153.
(21) Kretinin, A.; Cao, Y.; Tu, J.; Yu, G.; Jalil, R.; Novoselov, K.; Haigh, S.; Gholinia, A.; Mishchenko, A.; Lozada, M. Electronic properties of graphene encapsulated with different two-dimensional atomic crystals. *Nano Lett.* **2014**, *14* (6), 3270-3276.
(22) Pizzocchero, F.; Gammelgaard, L.; Jessen, B. S.; Caridad, J. M.; Wang, L.; Hone, J.; Bøggild, P.; Booth, T. J. The hot pick-up technique for batch assembly of van der Waals heterostructures. *Nat. Commun.* **2016**, *7* (1), 11894.
(23) Deng, S.; Berry, V. Wrinkled, rippled and crumpled graphene: an overview of formation mechanism, electronic properties, and applications. *Mater. Today* **2016**, *19* (4), 197-212.
(24) Sun, P.; Xiong, W.; Bera, A.; Timokhin, I.; Wu, Z.; Mishchenko, A.; Sellers, M.; Liu, B.; Cheng, H.; Janzén, E. Unexpected catalytic activity of nanorippled graphene. *Proc. Natl. Acad. Sci. U.S.A.* **2023**, *120* (12), e2300481120.
(25) Klimov, N. N.; Jung, S.; Zhu, S.; Li, T.; Wright, C. A.; Solares, S. D.; Newell, D. B.; Zhitenev, N. B.; Stroscio, J. A. Electromechanical properties of graphene drumheads. *Science* **2012**, *336* (6088), 1557-1561.
(26) Branny, A.; Kumar, S.; Proux, R.; Gerardot, B. D. Deterministic strain-induced arrays of quantum emitters in a two-dimensional semiconductor. *Nat. Commun.* **2017**, *8* (1), 15053.
(27) Ding, W.; Zhu, J.; Wang, Z.; Gao, Y.; Xiao, D.; Gu, Y.; Zhang, Z.; Zhu, W. Prediction of intrinsic two-dimensional ferroelectrics in In2Se3 and other III2-VI3 van der Waals materials. *Nat Commun* **2017**, *8*, 14956. DOI: 10.1038/ncomms14956.
(28) Zhou, Y.; Wu, D.; Zhu, Y.; Cho, Y.; He, Q.; Yang, X.; Herrera, K.; Chu, Z.; Han, Y.; Downer, M. C. Out-of-plane piezoelectricity and ferroelectricity in layered α-In2Se3 nanoflakes. *Nano Lett.* **2017**, *17* (9), 5508-5513.
(29) Cui, C.; Hu, W.-J.; Yan, X.; Addiego, C.; Gao, W.; Wang, Y.; Wang, Z.; Li, L.; Cheng, Y.; Li, P. Intercorrelated in-plane and out-of-plane ferroelectricity in ultrathin two-dimensional layered semiconductor In2Se3. *Nano Lett.* **2018**, *18* (2), 1253-1258.
(30) Yuan, S.; Luo, X.; Chan, H. L.; Xiao, C.; Dai, Y.; Xie, M.; Hao, J. Room-temperature ferroelectricity in MoTe2 down to the atomic monolayer limit. *Nat. Commun.* **2019**, *10* (1), 1-6.
(31) Deng, J.; Liu, Y.; Li, M.; Xu, S.; Lun, Y.; Lv, P.; Xia, T.; Gao, P.; Wang, X.; Hong, J. Thickness-Dependent In-Plane Polarization and Structural Phase Transition in van der Waals Ferroelectric CuInP2S6. *Small* **2020**, *16* (1), 1904529. DOI: https://doi.org/10.1002/smll.201904529.
(32) Liu, F.; You, L.; Seyler, K. L.; Li, X.; Yu, P.; Lin, J.; Wang, X.; Zhou, J.; Wang, H.; He, H. Room-temperature ferroelectricity in CuInP2S6 ultrathin flakes. *Nat. Commun.* **2016**, *7* (1), 1-6.
(33) Xu, D.-D.; Ma, R.-R.; Fu, A.-P.; Guan, Z.; Zhong, N.; Peng, H.; Xiang, P.-H.; Duan, C.-G. Ion adsorption-induced reversible polarization switching of a van der Waals layered ferroelectric. *Nat. Commun.* **2021**, *12* (1), 655.
(34) Chang, K.; Liu, J.; Lin, H.; Wang, N.; Zhao, K.; Zhang, A.; Jin, F.; Zhong, Y.; Hu, X.; Duan, W. Discovery of robust in-plane ferroelectricity in atomic-thick SnTe. *Science* **2016**, *353* (6296), 274-278.
(35) Bao, Y.; Song, P.; Liu, Y.; Chen, Z.; Zhu, M.; Abdelwahab, I.; Su, J.; Fu, W.; Chi, X.; Yu, W. Gate-tunable in-plane ferroelectricity in few-layer SnS. *Nano Lett.* **2019**, *19* (8), 5109-5117.

(36) Higashitarumizu, N.; Kawamoto, H.; Lee, C.-J.; Lin, B.-H.; Chu, F.-H.; Yonemori, I.; Nishimura, T.; Wakabayashi, K.; Chang, W.-H.; Nagashio, K. Purely in-plane ferroelectricity in monolayer SnS at room temperature. *Nat. Commun.* **2020**, *11* (1), 1-9.
(37) Chen, C.; Liu, H.; Lai, Q.; Mao, X.; Fu, J.; Fu, Z.; Zeng, H. Large-Scale Domain Engineering in Two-Dimensional Ferroelectric CuInP2S6 via Giant Flexoelectric Effect. *Nano Lett* **2022**, *22* (8), 3275-3282. DOI: 10.1021/acs.nanolett.2c00130.
(38) Das, S.; Tang, Y.; Hong, Z.; Gonçalves, M.; McCarter, M.; Klewe, C.; Nguyen, K.; Gómez-Ortiz, F.; Shafer, P.; Arenholz, E. Observation of room-temperature polar skyrmions. *Nature* **2019**, *568* (7752), 368-372.
(39) Zhang, Q.; Xie, L.; Liu, G.; Prokhorenko, S.; Nahas, Y.; Pan, X.; Bellaiche, L.; Gruverman, A.; Valanoor, N. Nanoscale bubble domains and topological transitions in ultrathin ferroelectric films. *Adv. Mater.* **2017**, *29* (46), 1702375.
(40) Yang, Y.; Zong, H.; Sun, J.; Ding, X. Rippling Ferroic Phase Transition and Domain Switching In 2D Materials. *Adv Mater* **2021**, *33* (49), e2103469. DOI: 10.1002/adma.202103469.
(41) Wang, H.; Zhang, L.; Han, J.; E, W. DeePMD-kit: A deep learning package for many-body potential energy representation and molecular dynamics. *Comput Phys Commun* **2018**, *228*, 178-184. DOI: 10.1016/j.cpc.2018.03.016.
(42) Larsen, A. H.; Mortensen, J. J.; Blomqvist, J.; Castelli, I. E.; Christensen, R.; Dułak, M.; Friis, J.; Groves, M. N.; Hammer, B.; Hargus, C. The atomic simulation environment—a Python library for working with atoms. *J. Phys. Condens. Matter* **2017**, *29* (27), 273002.
(43) Kolb, B.; Lentz, L. C.; Kolpak, A. M. Discovering charge density functionals and structure-property relationships with PROPhet: A general framework for coupling machine learning and first-principles methods. *Sci. Rep.* **2017**, *7* (1), 1-9.
(44) Wang, H.; Qian, X. Two-dimensional multiferroics in monolayer group IV monochalcogenides. *2D Mater.* **2017**, *4* (1), 015042.
(45) Morozovska, A. N.; Eliseev, E. A.; Dovbeshko, G. I.; Glinchuk, M. D.; Kim, Y.; Kalinin, S. V. Flexoinduced ferroelectricity in low-dimensional transition metal dichalcogenides. *Phys. Rev. B* **2020**, *102* (7), 075417.
(46) Morozovska, A. N.; Eliseev, E. A.; Shevliakova, H. V.; Lopatina, Y. Y.; Dovbeshko, G. I.; Glinchuk, M. D.; Kim, Y.; Kalinin, S. V. Correlation between corrugation-induced flexoelectric polarization and conductivity of low-dimensional transition metal dichalcogenides. *Physical Review Applied* **2021**, *15* (4), 044051.
(47) Shevliakova, H. V.; Yesylevskyy, S. O.; Kupchak, I.; Dovbeshko, G. I.; Kim, Y.; Morozovska, A. N. Flexoelectric and piezoelectric coupling in a bended MoS2 monolayer. *Symmetry* **2021**, *13* (11), 2086.
(48) Wu, J.; Bai, L.; Huang, J.; Ma, L.; Liu, J.; Liu, S. Accurate force field of two-dimensional ferroelectrics from deep learning. *Phys. Rev. B* **2021**, *104* (17). DOI: 10.1103/PhysRevB.104.174107.
(49) Mortazavi, B.; Javvaji, B.; Shojaei, F.; Rabczuk, T.; Shapeev, A. V.; Zhuang, X. Exceptional piezoelectricity, high thermal conductivity and stiffness and promising photocatalysis in two-dimensional MoSi2N4 family confirmed by first-principles. *Nano Energy* **2021**, *82*, 105716.
(50) Mortazavi, B.; Silani, M.; Podryabinkin, E. V.; Rabczuk, T.; Zhuang, X.; Shapeev, A. V. First-principles multiscale modeling of mechanical properties in graphene/borophene heterostructures empowered by machine-learning interatomic potentials. *Adv. Mater.* **2021**, *33* (35), 2102807.
(51) Likodimos, V.; Labardi, M.; Allegrini, M. Kinetics of ferroelectric domains investigated by scanning force microscopy. *Phys. Rev. B* **2000**, *61* (21), 14440.

(52) Liu, J.; Pantelides, S. Pyroelectric response and temperature-induced α-β phase transitions in α-In2Se3 and other α-III2VI3 (III= Al, Ga, In; VI= S, Se) monolayers. *2D Mater.* **2019**, *6* (2), 025001.

TOC Graphic

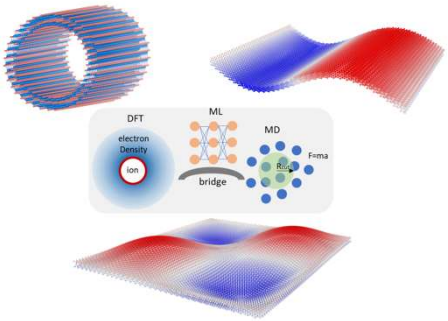

Supporting Information

Ferroelectric Domain and Switching Dynamics in Curved In_2Se_3: First Principle and Deep Learning Molecular Dynamics Simulations

[‡]Dongyu Bai[1], Yihan Nie[2,1], Jing Shang[3], Junxian Liu[1], Minghao Liu[1], Yang Yang[4], Haifei Zhan[2], Liangzhi Kou[1*] and Yuantong Gu[1*]*

1. School of Mechanical, Medical and Process Engineering, Queensland University of Technology, Brisbane, QLD 4001, Australia

2. College of Civil Engineering and Architecture, Zhejiang University, Hangzhou 310058, China

3. School of Materials Science and Engineering, Shaanxi University of Science and Technology, Xi'an, 710021 China

4. State Key Laboratory for Mechanical Behavior of Materials, Xi'an Jiaotong University, Xi'an 710049, China

1. Training Details of Deep Learning Potential

One parameter that affects the precision of the potential energy is loss function. Simplistic loss function, such as directly comparing the absolute error between the predicted value and real value, can cause the overfitting or poor transferability problems. The loss function here, including the physic information of force and virial. Shows in the following equation [1]:

$$L\left(p_e, p_f, p_v\right) = \frac{p_e}{N}\Delta E^2 + \frac{p_f}{3N}\sum_i |\Delta F_i|^2 + \frac{p_v}{9N}||\Delta v||^2 \quad \text{(S1)}$$

Where the three items ΔE, ΔF and Δv mean root mean square (RMS) error in energy, force, and virial. The three parameters p_e, p_f and p_v is the weights of this three information, which can change in the duration of optimization process. Its initial value depends on the trainer's setting.

Indeed, including above parameters, selecting different sets of hyperparameters can lead to variations in the performance of the potential energy model, impacting both accuracy and computational speed. Determining the optimal hyperparameters often involves a combination of conducting numerous experiments and applying physical intuition. In this work, the preset value of hyperparameters are referred to Wu's previous work 2, and the final set is chosen based on experiments. The table S1 below illustrates the effects of various hyperparameters choices on the potential energy.

After comprehensive consideration of both accuracy and training efficiency of the potential, the final set of hyperparameters for this work is as follows: the DeepMD-kit was employed as the training package with descriptor type "se_e2_a". To ensure the smoothness of the descriptor, a cutoff value of 6 Å was chosen, and the smoothed radius was set to 1Å. The embedding neural network used for training the descriptor had a size of (50,100,200). For the fitting neural network, the number of neurons in each layer was set to 300, 300, and 300, respectively. Here, we increased the weight P_e from 1 to 200, while gradually decreasing the weight P_f from 1000 to 1. Additionally, the virial weight P_v started at 0.02 and ended at 1. The learning rate was initially set to 0.001 and gradually decreased, reaching 3.51e-08 after a decay step of 20000. Finally, the training process consisted of 5000000 steps.

Table S1. Effect of hyperparameters settings on potential performance and computational costs*

Nodes	layers	P_e	P_f	P_v	Steps $\times 10^6$	Nodes Descriptor	MSE_e (meV/atom)	Training Time/ batch (s)
240	4	1-200	1000-1	0.02-1	1	25,50,100	110.51	8.23
240	3	1-200	1000-1	0.02-1	1	25,50,100	113.05	7.62
240	3	1-1000	1000-0.02	0.02-1	1	25,50,100	120.82	7.89
240	3	1-1000	1-0.02	0.02-1	1	25,50,100	115.19	8.79
240	3	0.1-200	1000-0.1	0.02-1	1	25,50,100	111.63	8.51
300	3	1-200	1000-1	0.02-1	1	25,50,100	72.88	8.1
300	3	1-200	1000-1	0.02-1	1	50,100,200	64.74	18.69
300	3	1-200	1000-1	0.02-1	5	50,100,200	32.32	10.22
350	3	1-200	1000-1	0.02-1	1	50,100,200	62.61	19.1
400	3	1-200	1000-1	0.02-1	1	25,50,100	72.42	9.82

*MSE_e: the mean squared error of energy

2. Model Construction

In order to address the issue of non-uniform deformations in 2D ferroelectric materials, we employed MATLAB to develop three distinct models with varying levels of complexity, including tube, mono sinusoidal, and orthogonal dual sinusoidal models. These models were designed to replicate the out-plane deformations resulting from corrugation in 2D ferroelectric materials (nanotube, ripple and bubble). Both the original and simplified versions of each model are displayed in Figure S1.

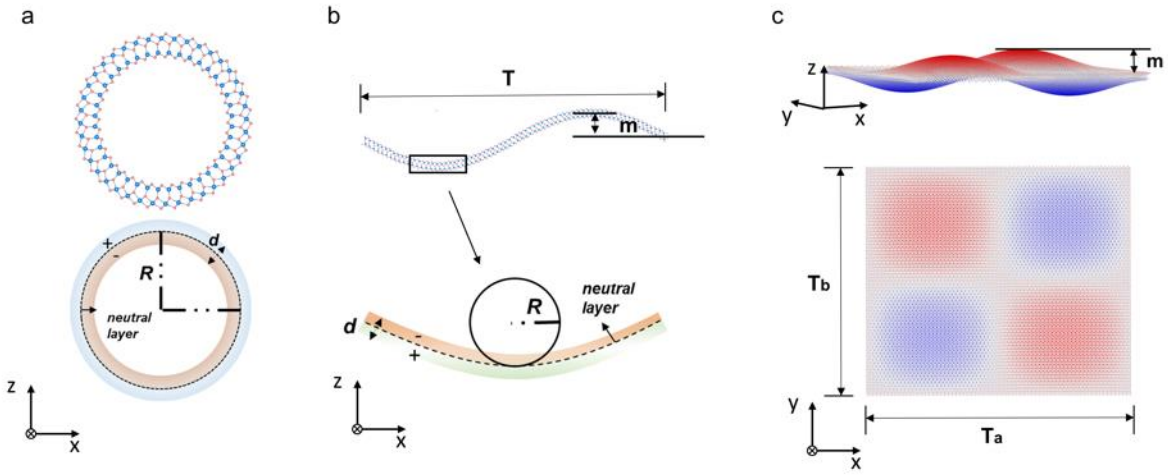

Figure S1. Three models and their simplified versions. (a) Nanotube model and its simplified version. (b) Mono sinusoidal model and its simplified version (ripple model). (c) Orthogonal dual sinusoidal model and its simplified version (bubble model).

In all three models, the neutral layer is located at the center of the innermost and outermost layers of selenium atoms. Atoms located in the inner state of compression are denoted by a minus sign, while atoms located in the outer state of tension are denoted by a plus sign. Initially, a pure tube model was constructed to investigate the effect of pure bending on the defects in polarization. The tube model is constructed using the following expression:

$$x^2 + z^2 = (R \pm d)^2 \tag{S2}$$

Where x and z represent the coordinates of atoms in that direction. R is the distance from the neutral layer to the center of the circle, and d is the distance between the atom layer and the neutral. (Shown in Figure S1(a)). And the d in figure is the distance between the outermost and innermost atoms.

We also considered the ripple deformation with the mono sinusoidal model shown in Figure S1(b), which can be described by the following equation:

$$\Delta z = m \times sin(\frac{2\pi}{\sqrt{3} l_a \times n_x} x) \tag{S3}$$

where x is the position in [1 0 0] direction, and Δz are the preset displacement of each atom in [0 0 1] direction according to the function of the neutral layer, m is the rippling amplitude, l_a is the periodic length along the x direction, and n_x is the lattice number in one period. R in Figure S1(b) is the radius of curvature at the vertex of the model, which is used to quantitatively analyze the degree of bending. Prior to calculation, the energy of

the model must be minimized, which usually does not significantly affect the model's structure but can eliminate the tensile strain in the x direction. However, for the mono sinusoidal model, energy minimization may alter the model size (the value of $T = \frac{2\pi}{\sqrt{3}l_a \times n_x}$), due to the presence of tensile strain along the x direction during construction. Therefore, in the subsequent data analysis, we will use the actual value of T to perform calculations.

The bubbling deformation is simulated with the dual sinusoidal shape, a new period deformation is added in y direction, where the crystal is affected by the gradient strain from multi-directions. We used 70 unit-cells along the x and y directions, containing 4,900 unit-cells and 24,500 atoms. Based on the findings of nanotubes and rippled monolayers, we pre-set the polarization to point upwards (downwards) at the crest (trough) of the bubble. The polarization and structures of the transition zone from the crest to the trough were determined through linear interpolation. The new model function is shown as:

$$\Delta z = m \times sin\left(\frac{2\pi}{\sqrt{3}l_a \times n_x}x\right) \times sin\left(\frac{2\pi}{l_b \times n_y}y\right) \quad \text{(S4)}$$

Similar to before, the variables x and y represent the coordinates along the corresponding direction. The value of T_a in Figure S1(c) is the angular frequency of model along x direction and shown as $\frac{2\pi}{\sqrt{3}l_a \times n_x}$ in equation S4, while T_b is the angular frequency of model along y direction and shown as $\frac{2\pi}{l_b \times n_y}$. Here, n_x and n_y denote the number of lattices on the x and y axis, and l_a and l_b are the lattice parameters along the x and y directions, respectively. Additionally, the parameter m still denotes the amplitude of the model.

3. Computational Details

3.1. DFT simulations

DFT simulation have been performed on microscale structure (Raduis = 22.60 Å) by using the Vienna Ab initio simulation package (VASP) [3]. Simulations are implemented within the Perdew-Burke-Ernzerhof (PBE) function [4] and generalized gradient approximation (GGA) [5] for the calculations of geometries optimization and the electron localization function (ELF) of microscale tube models. Then, the climbing-image nudge elastic band (CI-NEB) method [6] was adopted to calculate the energy barriers between polarization directions toward up and down under various in-plane strains by using the unit cell structures. In present simulations, the total energy and residual force were convergent to an accuracy of 10−5 eV and 10−2 eV/Å, respectively. Here, the plane-wave energy cutoff of 450eV was used. The

Brillouin zone was represented by a Monkhorst-Pack special k-point meshes [7] of 8 × 1 × 1 and 8 × 8 × 1 for micro tubes and unit cell structures, respectively. Besides, at least 15 Å of the vacuum layer were included in the non-periodic orientations to exclude the interlayer interactions between the neighbouring structures.

To exclude the impact of exchange correlation function, we did complementary simulations with different exchange correlation functions, including PBE, LDA, PBEsol and optPBE. It is found the trend of ferroelectric switching is very similar although the value of barrier is different to some degree. The main conclusion is not significantly affected by the choice of exchange functions.

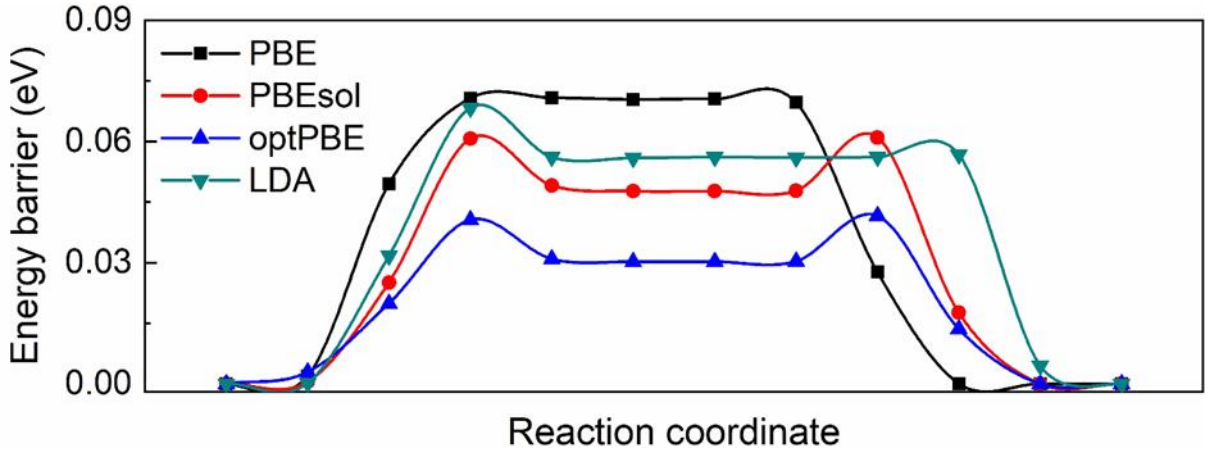

Figure S2. The comparison of energy barrier calculated by different exchange correlation function.

3.2. MD Simulations

The MD simulation is implemented by an open-source code, Large-Scale Atomic/Molecular Massively Parallel Simulator (LAMMPS) [8]. The potential energy employed in the simulation is trained by deep neural network, which can accurately simulate the 2D In_2Se_3 and its polarization switching on a larger scale.

In this simulation, two energy minimization methods were employed. The Polak-Ribiere version of the conjugate gradient (CG) algorithm was mainly used for tubes and mono sinusoids, while the damped dynamics method, described in the study by Bitzek et al., was utilized as a minimization method for dual sinusoidal models. The time step of all simulation was 0.001 picosecond. The tube simulation was performed in 1000000 steps and the sinusoidal simulation was performed in 200000 steps.

To ensure that the models retain their shape during relaxation, different external forces were applied during simulation. In the case of the tube model, two types of constraints were applied. Firstly, an external indentation force is applied only in the radial direction to maintain pure bending deformation, which mimics slip interaction with the substrate. Secondly, the positions of the external layer are fixed to mimic frictional interaction. Although the second constrain takes longer for the structure to relax to the ground state, it helps to maintain the structure with large deformation. The impact of these two methods will be discussed in the results section. The indenting force that be added to the outermost atom follows the equation:

$$F(r) = -K \times (r - R)^2 \tag{S5}$$

Where K is the specified force constant, r is the outer radius of the tube, and R is the radius of the indenter. Here, K and $(r - R)$ are equal to 10 and -0.08 Å, respectively.

For the shape of a mono sinusoidal during relaxation, the minimum z-coordinate atoms were fixed in the x direction. And the force added on the z direction is the following equation:

$$f(z) = -vk \times \left(z - m \times \sin\left(\frac{2\pi}{\sqrt{3}l'_a \times n_x}x\right) + va\right) \tag{S6}$$

Where z stands for the coordinates of the atom in z direction. m and n_x are the same parameters as in the model expression. l'_a is the lattice parameter after energy minimize. vk is the parameter that controls the value of applied force, like the elastic coefficient, here we set vk =1. va is the distance between the atoms and the neutral layer along the z direction.

As for the dual sinusoidal, a kind of similar force is applied to the lowest atoms:

$$f(z) = -vk \times \left(z - m_1 \times \sin\left(\frac{2\pi}{\sqrt{3}l_a \times n_x}x\right)\sin\left(\frac{2\pi}{l_b \times n_y}y\right) + va\right) \tag{S7}$$

In the analysis of MD simulation results, it is necessary to visualize the obtained results to intuitively display it. Two graphical visualization software OVITO [9] and VESTA [10] are used to visualize the relaxed trajectory structures.

4. Validation of Deep Learning Potential

To validate the accuracy of the DL potential, we conducted barrier calculations for two dynamic paths of In_2Se_3 polarization switching and the energy change of In_2Se_3 single

crystal under uniaxial stretching, employing the DL potential. Subsequently, we compared these results with DFT results. The outcomes of this comparative analysis are presented in Figure S3. The dynamic path of switching is derived from [11], while the DFT results for stretching are derived from [2].

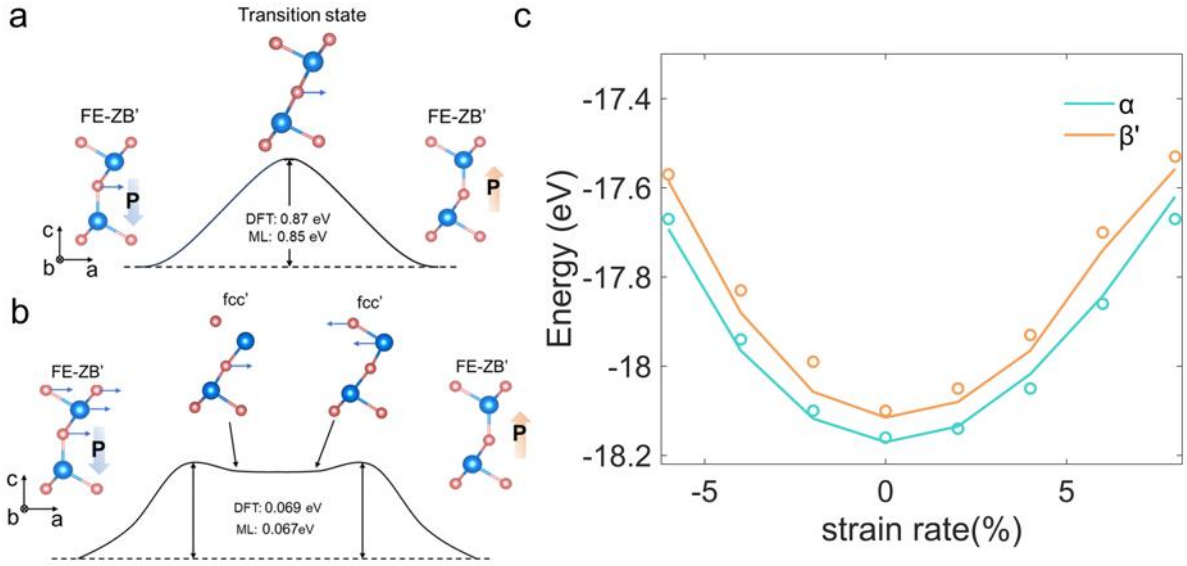

Figure S3. The comparison of DFT and ML results. (a,b) calculation of two kinetics pathways of In_2Se_3 polarization switching [11]. (a) One-step switching pathway with the movement of central Se. (b) Multi-step switching pathway with the movement of upper three layers. (c) The energy change curve of single In_2Se_3 lattice under uniaxial deformation in [1 0 0] and [0 0 1] direction. Circle points come from ML potential; solid lines are donated by DFT results that come from same source as database [2].

5. Flexoelectric effect

The polarization switching process involved in this work is a dynamic phenomenon caused by the laterally shift of central layer Se. This kinetics pathway can be induced by strain or an external electric field. The kinetics of the reversal process are shown in the MD trajectory file presented in Figure S4. To prove this process as the dominant mechanism governs the polarization switching process, we compare it with the potential influence of the flexoelectric effects.

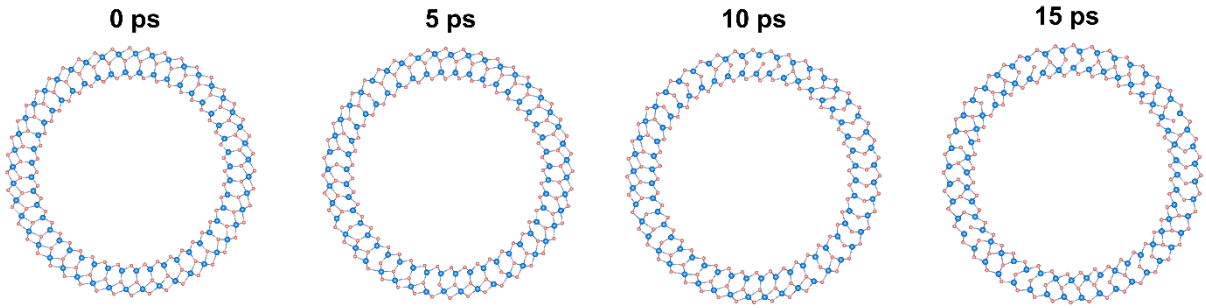

Figure S4. Polarization switching process of 24.96 Å nanotube at 300 K.

Here, we employ Zhuang et al.'s [12] method to investigate the flexoelectric effect in bending α-In_2Se_3, utilizing the nanotube models whose strain gradient are largest among three situations. A fixed super lattice size of 49.70 Å × 2.05 Å was adopted for all simulations. The polarization of this super lattice $\vec{p}$ is

$$\vec{p} = \frac{1}{v}\left(\sum_{i=1}^{n}(\vec{p}_{i0} + \vec{p}_{i1})\right) \tag{S8}$$

Where n is the number of units in the lattice, v is the volume of the super lattice, $\vec{p}_{i0}$ and $\vec{p}_{i1}$ are the original polarization and flexoelectric polarization at out-of-plane direction respectively. The $\vec{p}_{i1}$ is

$$\vec{p}_{i1} = \frac{1}{2}\,\mu^{z}K \tag{S9}$$

Where μ^{z} is the out-of-plane coefficient and K represents the strain gradient. Based on these two formulae, we can deduce the contribution η of the flexoelectric effect to polarization switching under the strain gradient by using two super lattices with opposite strain gradients as follows

$$\eta = \frac{|\vec{p}_{up} + \vec{p}_{down}|}{|\vec{p}_{up} - \vec{p}_{down}|} = \frac{|\vec{p}_{i1}|}{|\vec{p}_{i0}|} \tag{S10}$$

Based on function S10, we calculated the polarization of both up and down structures across a range of different radii of curvature. Figure S5 demonstrates the relation between η and

the radius, and the fitting curve aligns with the following equations:

$$\eta = \frac{\mu^z l_z}{kr} = \frac{5.491}{r} \tag{S11}$$

Where l_z represents the lattice constant in the z direction, corresponding to the thickness of the nanotube, and k is the constant coefficient. Notably, for the minimum radius 16.95 Å involved in this research, the flexoelectric effect contributes only 32.37% to polarization switching. Thus, the primary mechanism governing polarization reversion is the kinetic process involving the laterally shift of central layer Se.

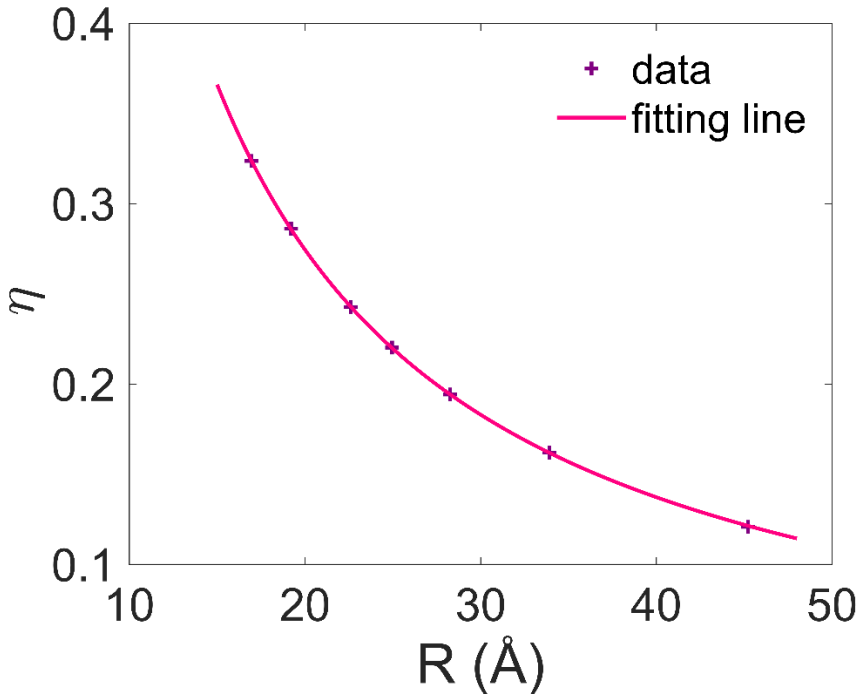

Figure S5. The change of η with radii and its fitting curve.

6. Further validation of DLMD potential

Using “dp-test” command in DeepMD-kit package to test the precision of Deep Learning potential within the training domain. The number of test frames is set to 30 and test results are shown in Figure S6.

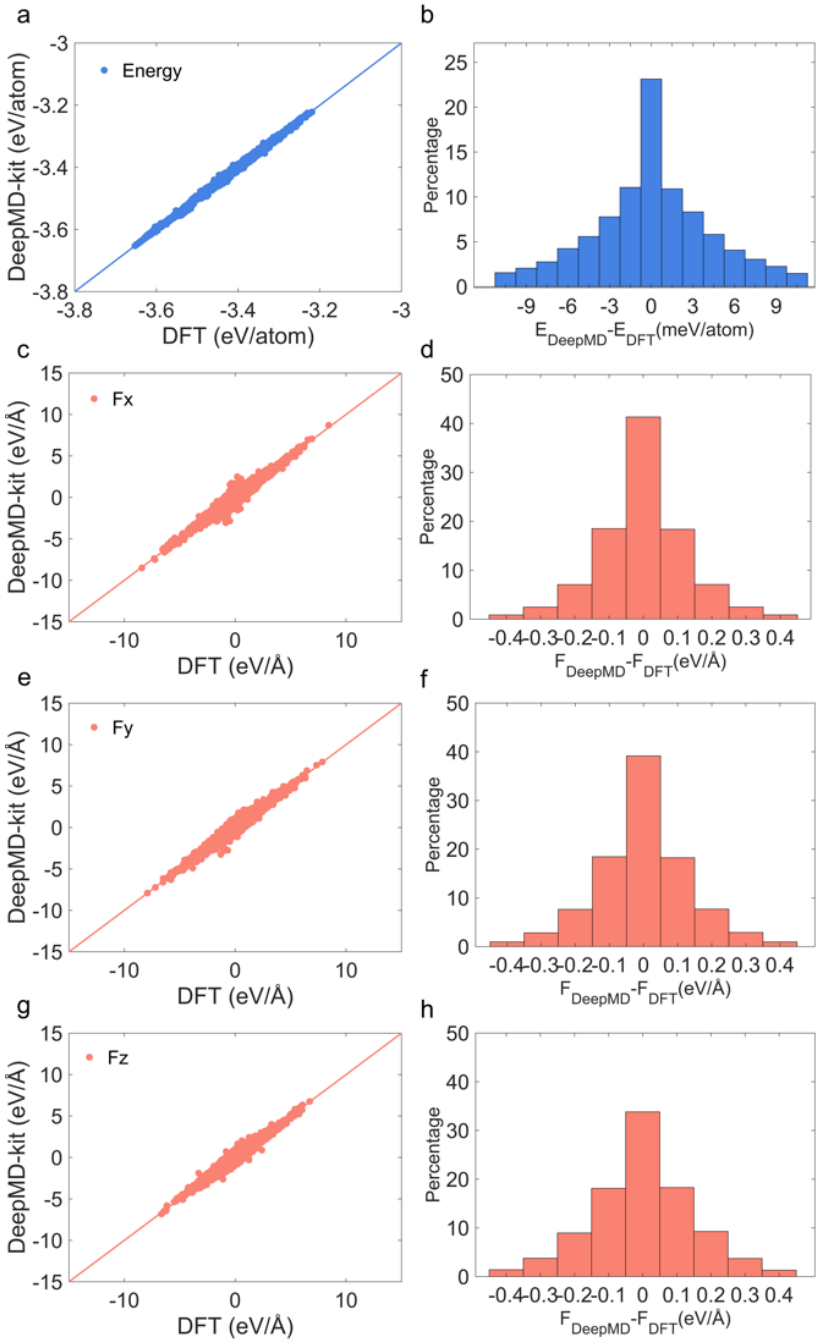

Figure S6. (a) Comparison of DFT and DLMD energy per atom. (b) The distribution of absolute error between DFT and DLMD energy (c,e,g) Comparison of DFT and DPMD atomic forces for configurations in the training database. (d,f,h) The distribution of absolute error between DFT and DLMD atomic force.

Using molecular dynamics simulation based on DL potential, we optimized the nanotube structure with a radius of 22.60 Å. Remarkably, the outcomes obtained from DL potential perfectly match the results calculated through DFT. The corresponding visualization of these results is presented in Figure S7.

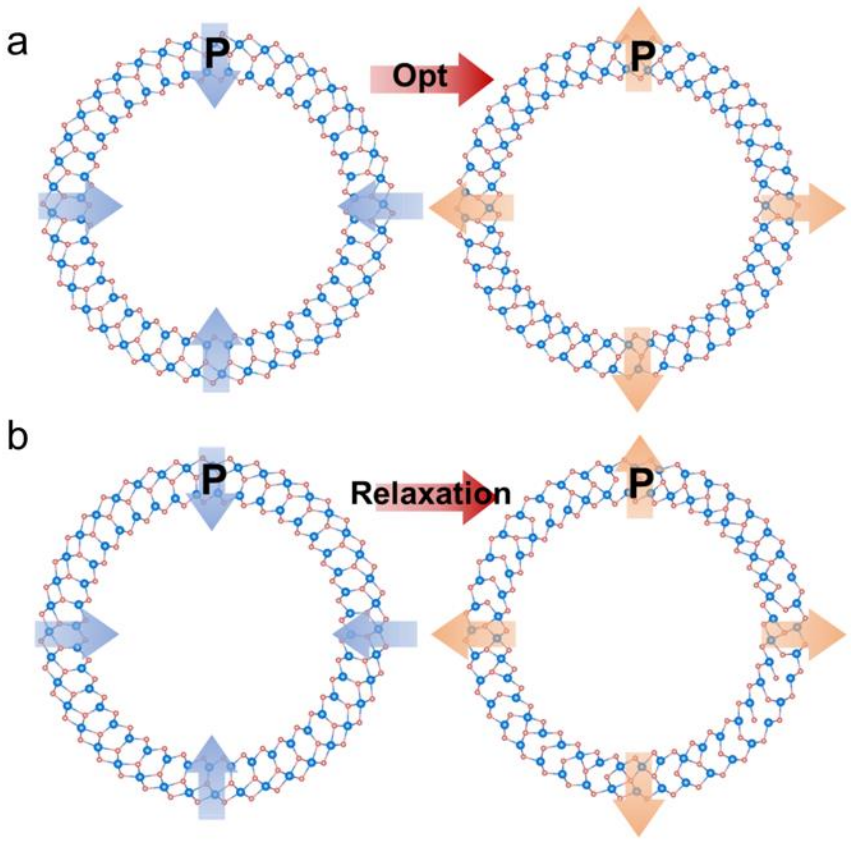

Figure S7. The comparison of DFT and MD results. (a) The structural optimizations of In_2Se_3 nanotube from P↑ and P↓ in DFT simulation (Ra = 22.60 Å). (b) The relaxation of In_2Se_3 nanotube from P↑ and P↓ in MD simulation with deep learning potential (Ra = 22.60 Å, T=300 K).

7. Dynamic of Polarization Switching under Pure Bending

The changes in energy before and after the structural relaxation of nanotubes with a radius of 28.25 Å were investigated at various temperatures (390 K, 400K, 450 K and 500 K).

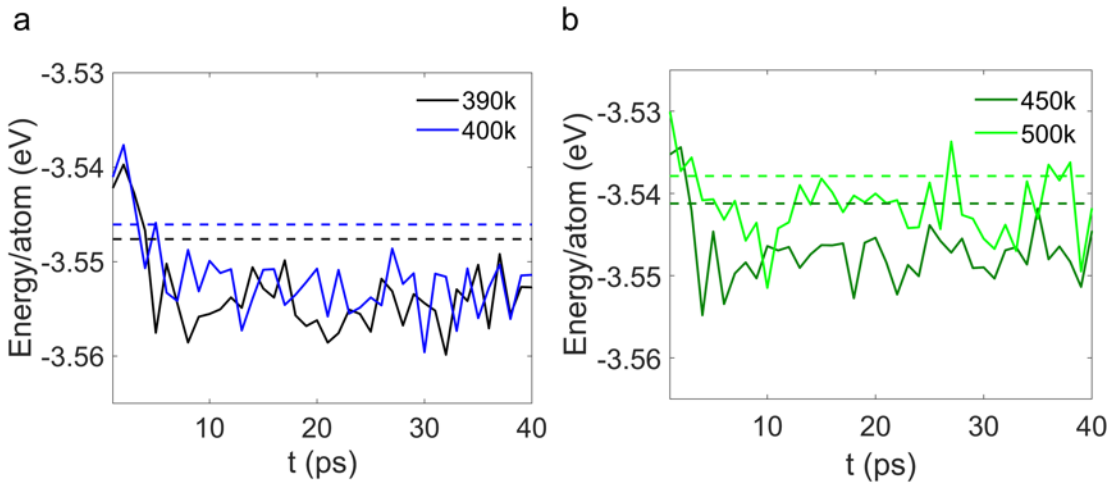

Figure S8. Energy-Time Diagram of System during Relaxation, Ra= 28.25 Å. (a) Comparison of switching time between 390 K and 400 K. (b) Comparison of switching time between 450 K and 500 K.

The impact of curvature on the switching dynamics at 300 K was examined, and Figure S8a complements the time-dependent change of energy for nanotubes with radii of 16.95 Å and 19.21 Å. The results reveal that the switching time is notably faster for the model with the smaller radius, consistent with the trend observed in Figure 2b.

To ensure the results are not influenced by constraints (indenter's strength) applied to the outermost atoms during relaxation, Figure S8b investigates the effect of curvature on the switching dynamics at 300 K without constraints. For this analysis, the models with radius of curvature ranging from 33.90 Å to 67.80 Å are selected to maintain the nanotube's shape. The findings demonstrate that while the energy barrier and switching time are affected under constraint conditions, the trend of accelerated switching with increasing curvature remains independent of the intender's strength.

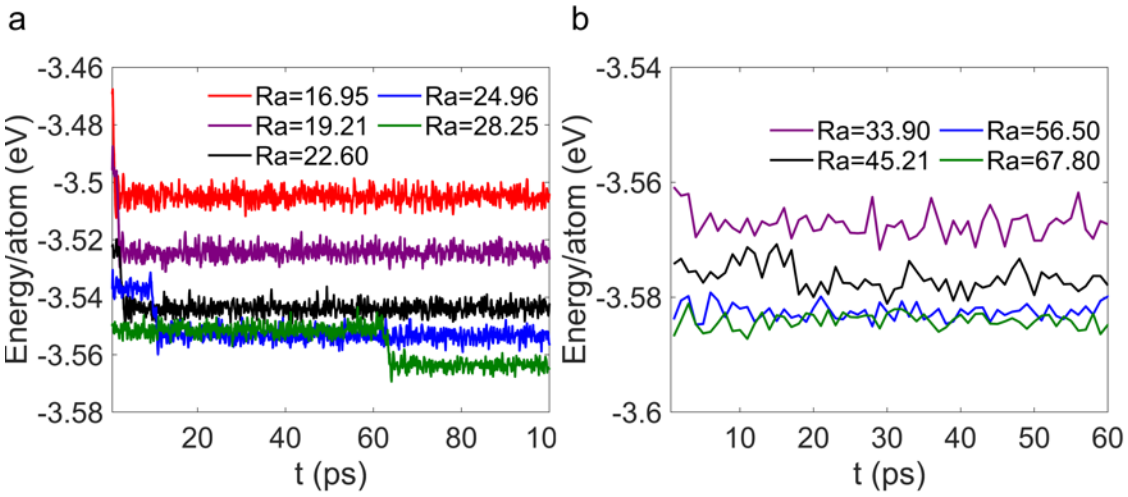

Figure S9. Energy-Time Diagram of System during Relaxation, T=300 K. (a) Comparison of Energy difference of different radii (from Ra=16.95 Å to 28.25 Å) with indenter force. (b) Comparison of Energy difference of different radii (from Ra=33.90 Å to 67.80 Å) without indenter force.

8. Dynamic of Polarization Switching under Ripple Deformation

The factors influencing polarization switching in ripples were thoroughly analyzed, and the switching speed was measured in various regions under different ripple amplitudes and temperatures. Here, the ripple amplitude (m) is set to 15 and 20, and the intended distribution of ripples at temperatures of 300 K and 550 K is illustrated in Figure S10. In the figure, the red color denotes the direction of polarization along the [0 0 1] direction, while the blue color represents the direction of polarization along the [0 0 -1] direction.

To perform a numerical analysis of the above discussion, the autocorrelation functions of each region were obtained under varying temperatures and amplitudes (Figure S11).

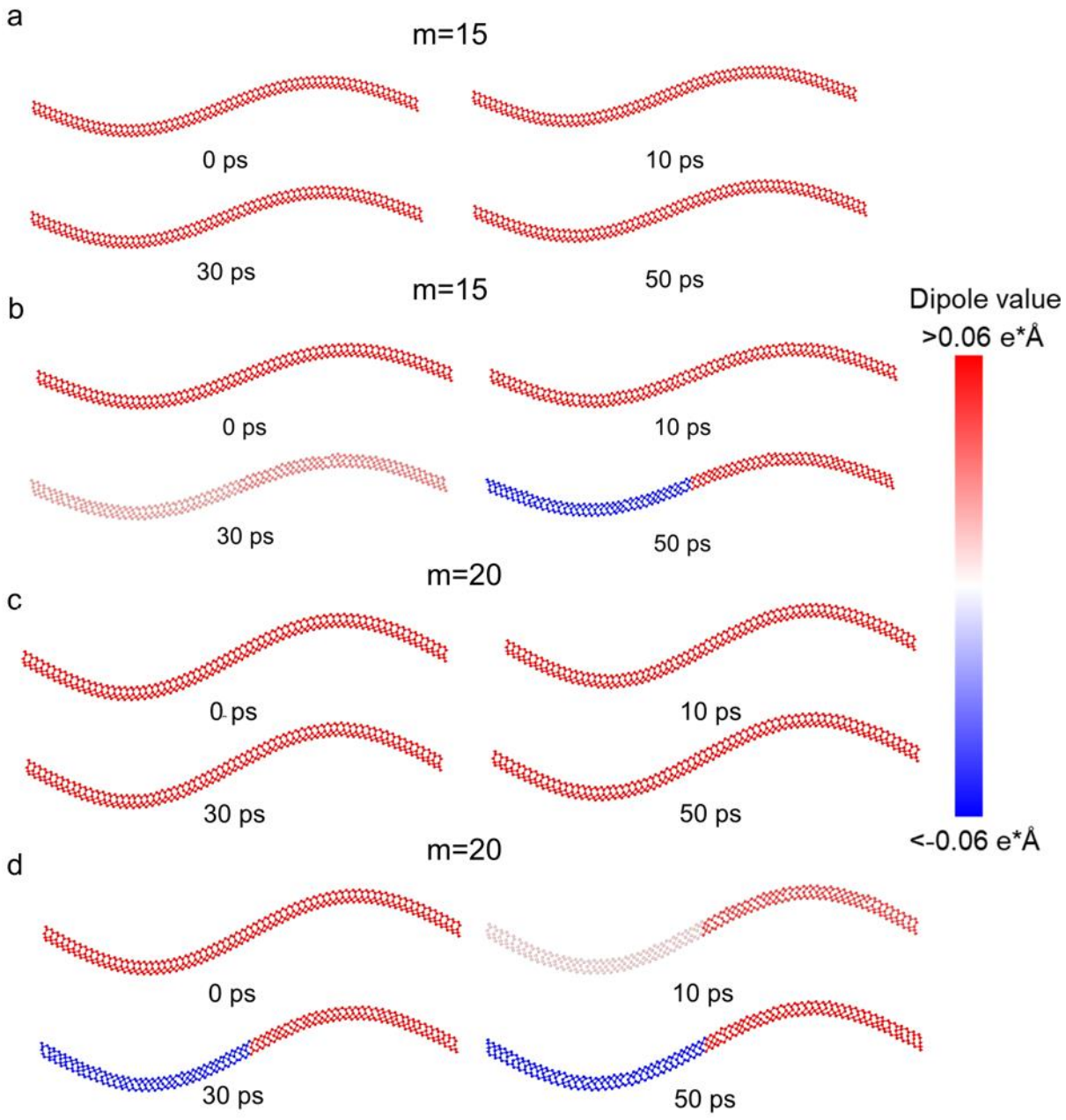

Figure S10. Dipole moment value of different region during relaxation of ripple model. (a) The variation of dipole moment value with time, where m = 15; T = 300 K. (b) The variation of dipole moment value with time, where m = 15; T = 550 K. (c) The variation of dipole moment value with time, where m = 20; T = 300 K. (d) The variation of dipole moment value with time, where m = 20; T =550 K.

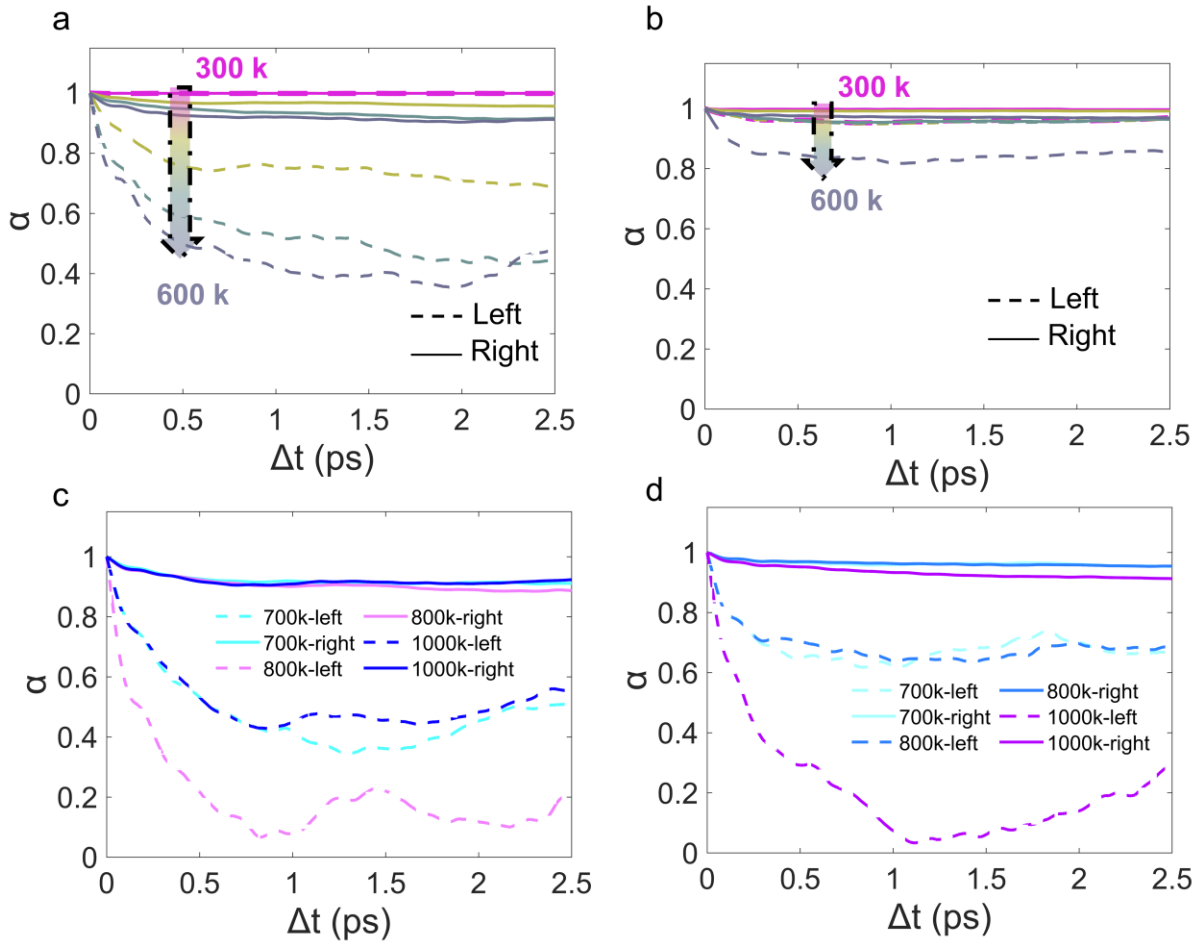

Figure S11. The autocorrelation function of regional (left and right) dipole moment of ripple model. (a) m = 15, the temperature is from 300 K to 600 K. (b) m = 20, the temperature is from 300 K to 600 K. (c) m = 15, the temperature is 700, 800, 1000 K. (d) m = 20, the temperature is 700, 800, 1000 K.

9. Dynamic of Polarization Switching under Bubble Deformation

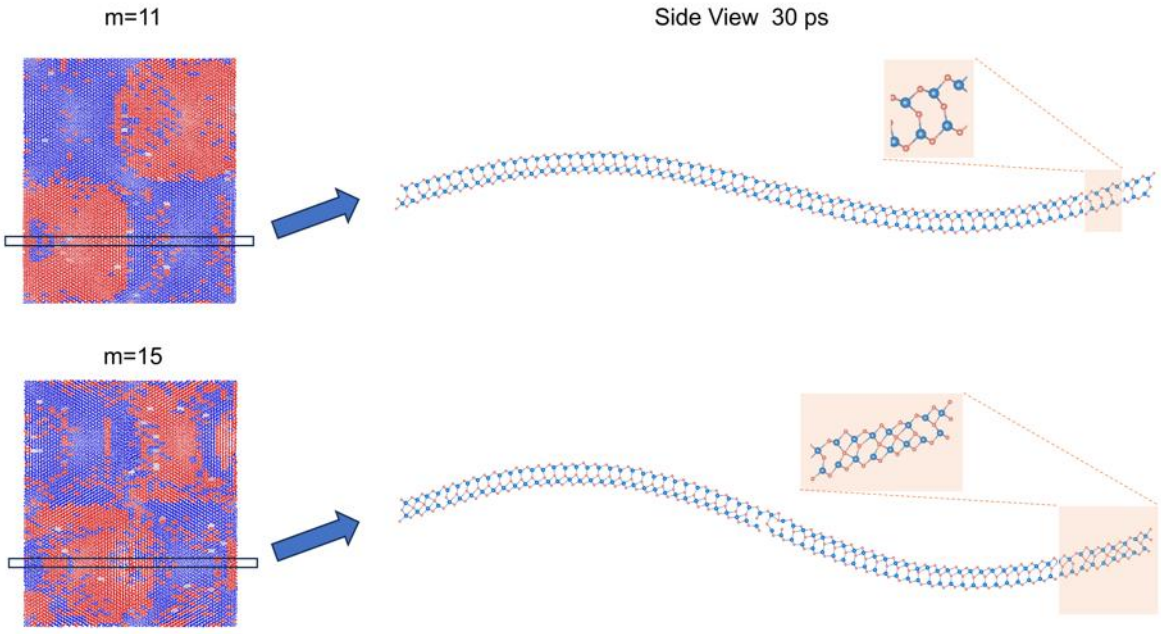

Figure S12. The configuration in the boundary between neighboring ferroelectric domains in bubble models, m=11 and 15.

In Figure S12, we observe the configuration between neighboring ferroelectric domains in the bubble model at varying amplitudes (m=11, m=15). Notably, the composition of this structure primarily consists of the β phase, and as the amplitude increases, the boundary domain expands, corresponding to a reduction in the size of the polarization domain.

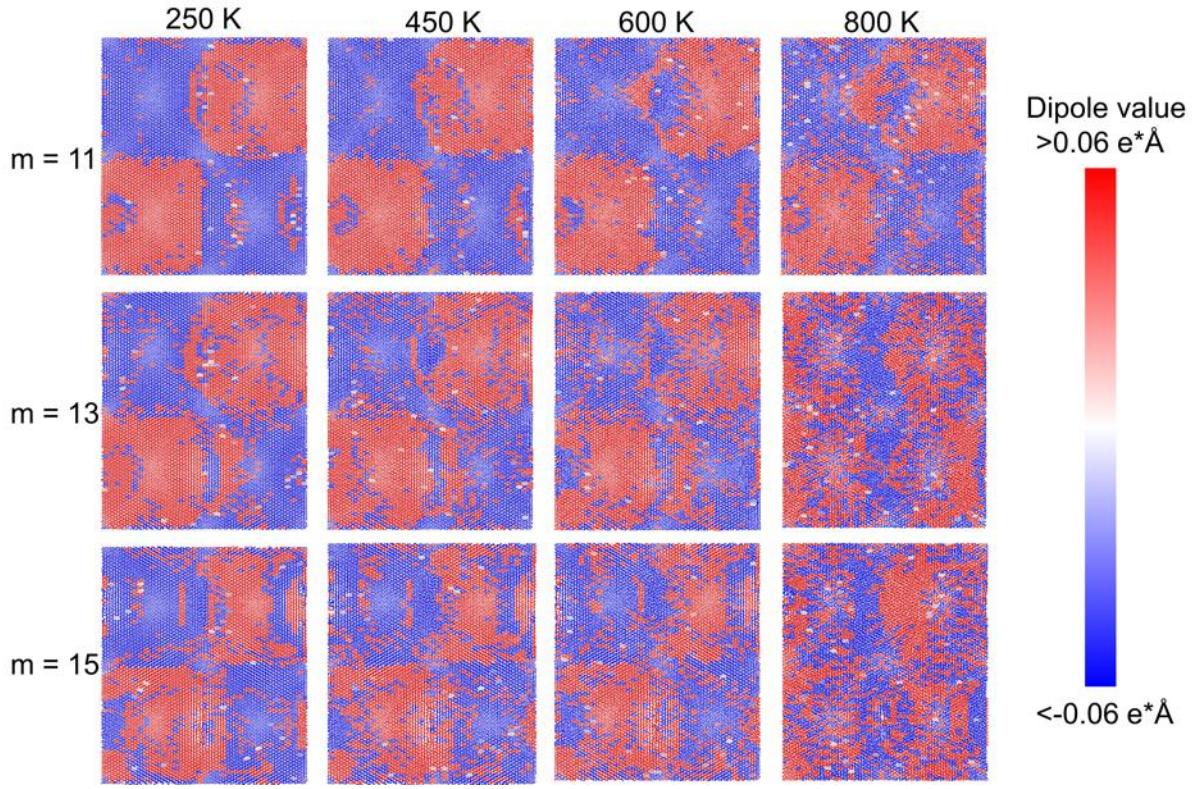

Figure S13. The dipole moment distribution during relaxation of bubble model of different m and temperature (relaxation time is 50 ps).

Figure S13 illustrates the impacts of different temperatures and amplitudes on the polarization distribution in the bubble model. The red region represents the polarization direction along the [0 0 1], while the blue region represents the polarization direction along the [0 0 -1].

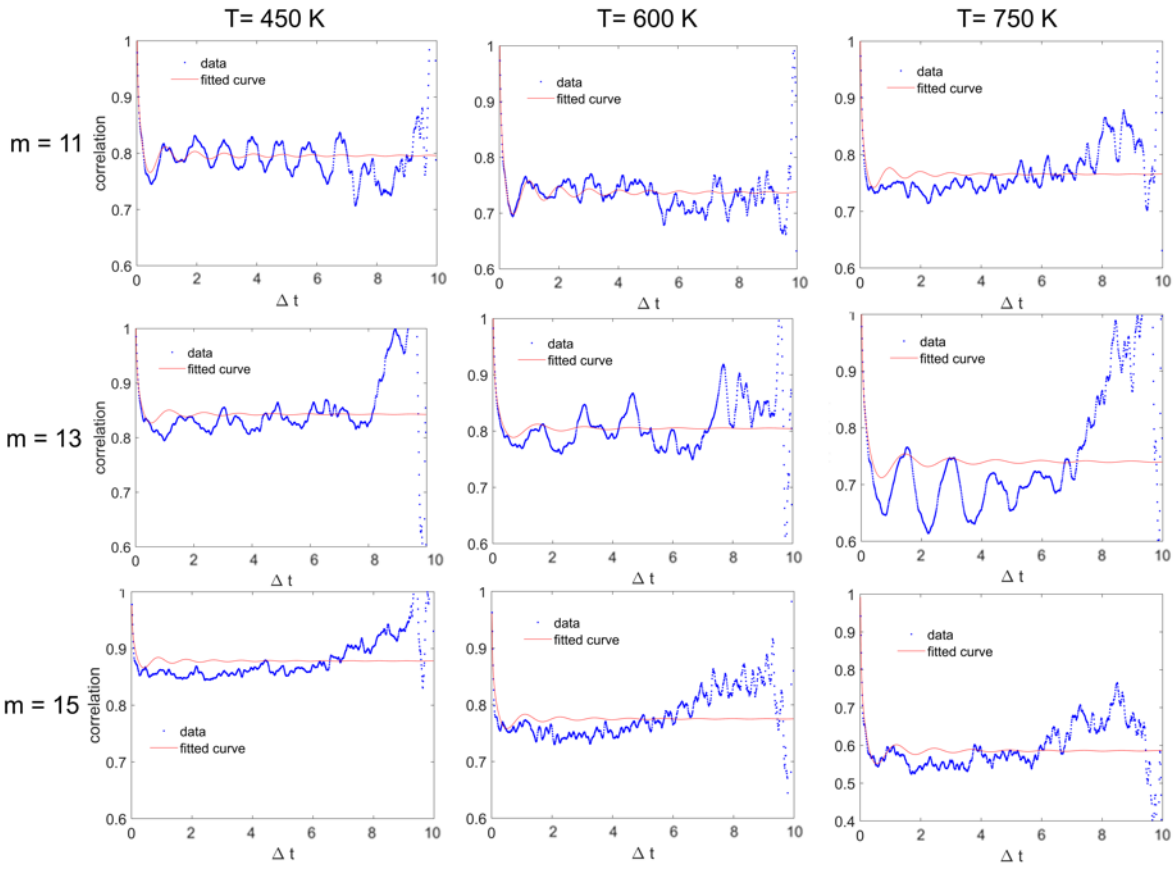

Figure S14. Bubble model: the autocorrelation and its fitting curve of the dipole moment at different temperature. The autocorrelation and its fitting curve of the dipole moment in m = 11, m = 13, and m = 15 model, where temperature is 450 K, 600 K, and 700 K.

To calculate the autocorrelation function for the near-vertex region. Specifically, we selected 64 points in four 36.45*49.91 angstroms rectangles at the peaks (troughs) of the model. Figure S14 displays autocorrelation functions along with their fitting curves for various specific amplitudes and temperatures.

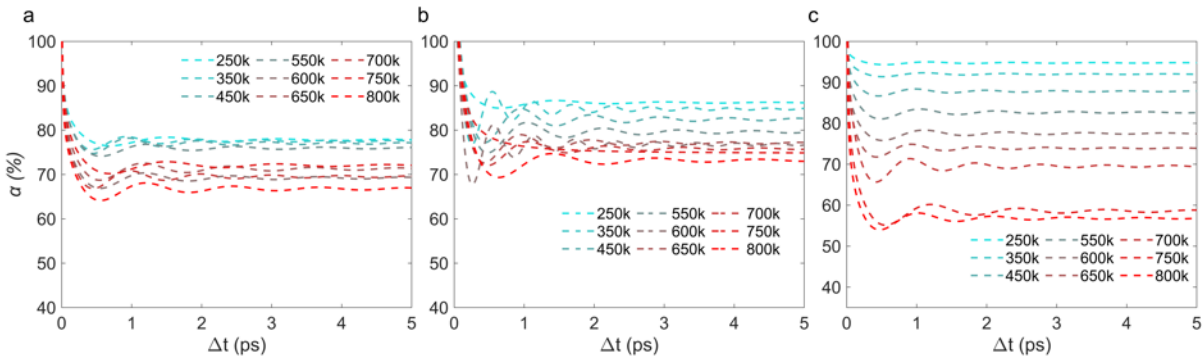

Figure S15. Bubble model: the autocorrelation of the dipole moment at different temperature. (a) the autocorrelation of the dipole moment in m = 11 model, the temperature is from 250 K to 800 K. (b) the autocorrelation of the dipole moment in m = 13 model, the temperature is from 250 K to 800 K. (c) the autocorrelation of the dipole moment in m = 15 model, the temperature is from 250 K to 800 K.

The autocorrelation functions under m=11, 13, and 15 are presented in Figure S15. We observed that under the same strain gradient condition, the correlation is lower under higher temperatures, indicating that the structural stability is negatively affected by environmental temperature.

Reference

(1) Wang, H.; Zhang, L.; Han, J.; E, W. DeePMD-kit: A deep learning package for many-body potential energy representation and molecular dynamics. *Comput Phys Commun* **2018**, *228*, 178-184. DOI: 10.1016/j.cpc.2018.03.016.

(2) Wu, J.; Bai, L.; Huang, J.; Ma, L.; Liu, J.; Liu, S. Accurate force field of two-dimensional ferroelectrics from deep learning. *Phys. Rev. B* **2021**, *104* (17). DOI: 10.1103/PhysRevB.104.174107.

(3) Kresse, G.; Furthmüller, J. Efficient iterative schemes for ab initio total-energy calculations using a plane-wave basis set. *Phys. Rev. B* **1996**, *54* (16), 11169.

(4) Perdew, J. P.; Burke, K.; Ernzerhof, M. Generalized gradient approximation made simple. *Phys. Rev. Lett.* **1996**, *77* (18), 3865.

(5) Langreth, D. C.; Mehl, M. Beyond the local-density approximation in calculations of ground-state electronic properties. *Phys. Rev. B* **1983**, *28* (4), 1809.

(6) Henkelman, G.; Uberuaga, B. P.; Jónsson, H. A climbing image nudged elastic band method for finding saddle points and minimum energy paths. *J. Chem. Phys.* **2000**, *113* (22), 9901-9904.

(7) Monkhorst, H. J.; Pack, J. D. Special points for Brillouin-zone integrations. *Phys. Rev. B* **1976**, *13* (12), 5188.

(8) Plimpton, S. Fast parallel algorithms for short-range molecular dynamics. *J. Comput. Phys.* **1995**, *117* (1), 1-19.

(9) Stukowski, A. Visualization and analysis of atomistic simulation data with OVITO–the Open Visualization Tool. *Model Simul Mat Sci Eng.* **2009**, *18* (1), 015012.

(10) Momma, K.; Izumi, F. VESTA 3 for three-dimensional visualization of crystal, volumetric and morphology data. *J. Appl. Crystallogr.* **2011**, *44* (6), 1272-1276.

(11) Ding, W.; Zhu, J.; Wang, Z.; Gao, Y.; Xiao, D.; Gu, Y.; Zhang, Z.; Zhu, W. Prediction of intrinsic two-dimensional ferroelectrics in In2Se3 and other III2-VI3 van der Waals materials. *Nat Commun* **2017**, *8*, 14956. DOI: 10.1038/ncomms14956.

(12) Zhuang, X.; He, B.; Javvaji, B.; Park, H. S. Intrinsic bending flexoelectric constants in two-dimensional materials. *Phys. Rev. B* **2019**, *99* (5), 054105.